On numerical aspects of different updating schedules for tracking fracture path in strain localization modeling

S.M. Parvaneh, C. D. Foster*

Department of Civil and Materials Engineering, University of Illinois at Chicago, Chicago, IL 60607, U.S.A.

Abstract

A comparative study is performed that investigates numerical features of different schedules, end-of-step vs. within iterations, for updating fracture path by employing the local and global tracking strategies. Embedded strong discontinuities within an enhanced finite element framework are used to model propagating discontinuities and fracture behavior of quasi-brittle materials. It is shown that end-of-step updating, which is a standard, can cause inaccuracies in peak strength and fracture energy for large time steps. Updating within iterations rectifies the accuracy issues, but at the expense of an increased computational cost. Both schedules yield comparable performance as the step size is refined.

Keywords: cohesive zone modeling, enhanced finite element, fracture path, tracking strategy, updating schedule

1. Introduction

Materials subjected to a certain loading conditions are predisposed to exhibit considerable deformation across narrow regions compared to the majority of the body. This phenomenon is generally termed as localized deformation. Tensile and shear fractures in brittle rocks and concrete, and shear bands in sands are examples of geomaterials in which this type of deformation is observed. Much work has been carried out in recent decades aiming to identify the criteria for onset of localization as well as the mechanics of localizing and fully localized bands.

The entire spectrum of localized deformation can roughly be classified into two families based upon their geometry, i.e., the character of the deformation in the localized region. The first group is characterized by localization bands with narrow but finite width.

---

*Corresponding author. *Address:* 2095 Engineering Research Facility, 842 W. Taylor Street (M/C 246), Chicago, Illinois 60607-7023, U.S.A. *Phone:* +1 (312) 996-8086.
   Email address: `fosterc@uic.edu` (C. D. Foster)

Nomenclature

Latin characters

$\boldsymbol{b}$	body force
$\boldsymbol{B}$	strain-displacement matrix
c	prescribed elastic modulus term
$\boldsymbol{C}$	modulus tensor
d	prescribed displacement (mm)
$\boldsymbol{d}$	unknown displacement vector
E	Young's modulus (MPa)
f	softening function
$f_1,\ f_2$	quantities representing balance equations
f_t	tensile strength (MPa)
G	shear modulus (MPa)
G_F	fracture energy (N/mm)
H	Heaviside function
$\boldsymbol{K}$	stiffness matrix/thermal conductivity tensor
$\boldsymbol{l}$	surface orientation
max	maximum
$\boldsymbol{n}$	normal to discontinuity surface
$\boldsymbol{N}$	finite element shape function matrix
$\boldsymbol{q}$	conduction flux-like vector (W/m^2)
$\boldsymbol{r}$	localization residual
$\boldsymbol{R}$	standard residual
S	discontinuity surface
t	time
$\boldsymbol{t}$	traction
T	temperature
tol	relative convergence tolerance
$\boldsymbol{u}$	displacement field
$\bar{\boldsymbol{u}}$	regular displacement
$\tilde{\boldsymbol{u}}$	conforming displacement
$\boldsymbol{w}$	displacement jump
$\tilde{w}$	maximum of displacement jump magnitude
$\boldsymbol{x}$	global coordinates of a material point

Greek characters

Γ	material boundary
δ	Dirac delta distribution
ϵ	isotropic algorithmic conductivity
$\boldsymbol{\varepsilon}$	strain field
θ	angle
ν	Poisson's ratio

$\boldsymbol{\nu}$	outward normal to material boundary
$\boldsymbol{\sigma}$	stress field
Ω	material domain

Sub/Superscripts, abbreviations, and special functions

$+$	active domain
$-$	inactive domain
$*$	prescribed value
c	critical
$conf$	conforming part
$conv$	converged
CST	constant stain triangular
dd	derivative of standard residual with respect to displacement
dw	derivative of standard residual with respect to jump
e	(subscript) element
e	(superscript) elastic
f^h	arbitrary smooth function
h	finite element discretization
loc	localized
n	normal component
reg	regular part
s	(subscript) sliding component
s	(superscript) symmetric part of a tensor
wd	derivative of localization residual with respect to displacement
ww	derivative of localization residual with respect to jump
x	along x-axis in a global cartesian coordinate system
xx, xy, yy	identifiers for strain tensor components
y	along y-axis in a global cartesian coordinate system

The displacement field throughout the body has no jumps or discontinuities though there is intense straining at the localized region. The strain field may become discontinuous. This type of discontinuity is generally termed as weak discontinuity [Simo et al., 1993], which can be observed in shear, compaction, and dilation bands in ductile materials. The second group, which is referred to as a strong discontinuity [Simo et al., 1993], includes localization surfaces with zero thickness. Localized deformations of this type have discontinuities or jumps in the displacement field at the localization surface that results in unbounded strain. Tensile fractures in rock, mortar, and concrete are examples of this type.

Modeling localized deformation is recognized to be a challenging task, partially because the governing equations of equilibrium may lose ellipticity, which results in a spurious mesh dependence. Different techniques have been developed in recent decades to surmount the associated issues. Viscous regularization (e.g. [Needleman, 1988]), nonlocal (e.g. [Jirásek and Rolshoven, 2003]) and gradient plasticity (e.g. [Manzari and Regueiro, 2005]), and Cosserat continua (e.g. [Cosserat and Cosserat, 1909; De Borst and Sluys, 1991; Khoei et al., 2010]) are all within a class of techniques where auxiliary information is added to the governing PDEs to ensure ellipticity and remove spurious mesh dependence of the solution. These techniques require knowledge of a characteristic length scale to complete their formulation. In addition, several elements across the thickness of the localized region are often necessary to accurately capture the deformation of the localized region. This requirement can make the simulation computationally expensive, especially when the location of the localized region is not known a priori.

An alternative approach is using the other class of techniques where localized region is treated as a surface with zero thickness. This assumption has some strong physical justifications for geomaterials as pointed out in [Borja and Regueiro, 2001]. Cohesive surface elements [Regueiro et al., 2005] and continuum strong discontinuity approach [Simo et al., 1993] are among the developed methods of this class [Foster, 2006]. Studies on other element technologies within this class can be found in [Jirásek, 2000] and [Oliver et al., 2003]. The extended finite element method [Belytschko et al., 2001; Moës and Belytschko, 2002; Zi and Belytschko, 2003; Khoei et al., 2008; Mohammadnejad and Khoei, 2013; Khoei, 2014] and generalized finite element method [Strouboulis et al., 2000; Duarte et al., 2000, 2001; Bia-

banaki and Khoei, 2012] are other numerical techniques to mention that provide the tools for the analysis of problems characterized by discontinuities [Fries and Belytschko, 2010]. Among other numerical methods developed to model localized deformation, element-free methods, in which only nodal data and a description of the geometry are required to resolve PDEs [Belytschko et al., 1994], have been used for modeling localization. Like finite element method, element-free methods without proper physics do not provide formulations for capturing softening response in a localization phenomenon. However, they are characterized by some numerical features that make them suitable for modeling strong discontinuities. Within this class, enriched Element-Free Galerkin formulation [Fleming et al., 1997], the Reproducing Kernel Particle Method [Liu et al., 1995; Klein et al., 2001; Boyce et al., 2014], the Gradient Reproducing Kernel Particle Method [Hashemian and Shodja, 2008], and smoothed-particle hydrodynamics [Batra and Zhang, 2004] are among the developed methods. A number of reviews regarding these methods can be found in [Belytschko et al., 1996; Liu et al., 1996, 1999; Chen et al., 2011]. In this study, an enhanced element method closer to the second aforementioned class of methods (continuum strong discontinuity approach) is used, specifically following the element technology in [Foster et al., 2007].

Within the class of inter-element discontinuities in finite elements, there should be a mechanism to trace the propagation of the localized deformation. Different methods have been proposed for such purpose, which can be generally classified into two main groups: The local tracking strategy, as elaborated by [Foster et al., 2007] and the global tracking strategy, as described by [Oliver et al., 2002]. These two approaches are referred to as *band tracking strategies* or simply *tracking strategies* throughout the paper, and will be described in more detail in Section 5.

In addition to setting up a framework for detecting the onset of localization, determining surface orientation, finding the displacement jumps, and selecting a tracking strategy, one needs to decide at what points of the simulation the tracking algorithm should be carried out. This is often chosen to be at the end of each time step. While such scheduling is well recognized as an approximation, the magnitude of the approximation has not been quantified, nor many alternatives investigated. Typical reasons for making such selection are simpler implementation and more robustness, since all tracking estimations will then be based upon

the converged displacement solution of each time step. This scheduling is capable of handling band evolution analysis accurately provided that step size is controlled to be small enough for the given evolution of the crack pattern. Inaccurate predictions may occur for complex evolution patterns, for example, intense changes in band orientation or rapid propagation of the band. An alternative approach will then be performing the tracking algorithm, along with updating band information by the end of each global iteration within a given time step. This updating schedule is relatively more complicated to implement; however, it allows the evolution of localization bands to be determined within the iterations. This technique enables the algorithm to track the band evolution more accurately, but in expense of an increased computational cost. Creating a robust framework to model a localized deformation is an essential part of its computational simulation. The objective of this study is to examine accuracy and robustness of the band evolution algorithms and the aforementioned updating schedules. The question to be answered is that how the timing of performing a band tracking strategy should be selected; either based on incrementing the simulation time (at the end of each time increment), or emerging from nonlinear iterative solution algorithm for a given time interval (at the end of each global iteration within a given time increment). These two approaches are referred to as *band updating schedules* or simply *updating schedules* within this study.

In this article, localization is initiated when the maximum principal stress exceeds a given value, the tensile strength. The orthogonal direction to maximum principal stress is taken as the orientation of the localized surface. Finally, a traction-separation relationship in the spirit of damage mechanics is implemented to determine displacement jumps along localization bands. The bulk material away from the localized surface is assumed to be linear elastic. This model is simple but robust enough to allow us to focus on the numerical evolution and updating schedules. Formulations are developed for quasi-static problems under the assumption of infinitesimal deformation to keep resulting algorithms within a simple context. Although the continuum strains generally remain small, the finite strain formulation properly accounts for the local large strains and rotations accompanying separation of discontinuity surface interfaces. Examining robustness, quantifying accuracy, and evaluating simulation time for each updating schedule are carried out. The comparative study, therefore, provides a

6

framework for understanding observed differences between the implemented schedules, along with advantages and drawbacks of each.

Throughout the paper, vector and tensor quantities are written in boldfaced symbolic notation. Scalar quantities are not boldfaced. The inner product of two vectors or two second-order tensors is written as $\boldsymbol{a} \cdot \boldsymbol{b}$. The contraction of the innermost two indices of two tensors is written as $\boldsymbol{c} : \boldsymbol{d}$. The outer product is denoted as $\boldsymbol{e} \otimes \boldsymbol{f}$. Tensor operators are also used, including $\boldsymbol{\nabla}^s$ for symmetric gradient.

The remainder of the paper is structured as follows: kinematics for small strain deformation with embedded strong discontinuities are reviewed in Section 2. The traction-separation model is presented in Section 3. Implementation of the model within an enhanced finite element context is elaborated in Section 4, along with some calculation procedures for element-level displacement jumps. Band tracking strategies are discussed in Section 5. Numerical simulations, comparative studies, and concluding remarks are provided in Sections 6 and 7. Finally, Appendix A provides the residual expression for balance on the discontinuity surface in matrix form for numerical implementation purposes and derivation of its derivatives with respect to jump terms, needed for nonlinear numerical solution of governing equations. Flowcharts are also presented in this appendix that describe the implementation of different updating schedules for a given tracking strategy.

2. Kinematics

The kinematics of a body Ω with displacement jumps added to the smooth displacement field across a discontinuity surface S as depicted in Fig. 1a require implementing auxiliary enhancements to capture the introduced jumps. The reader is referred to [Simo et al., 1993; Armero and Garikipati, 1996; Borja, 2000] for detailed mathematical formulations of such enhancements. For the purpose of this paper, the formulations are developed under the assumption of infinitesimal deformation. The discontinuous displacement may then be defined as

$$\boldsymbol{u} = \bar{\boldsymbol{u}} + H_S \boldsymbol{w} \tag{1}$$

where $\bar{\boldsymbol{u}}$ represents the regular part of the displacement conforming to the smooth deformation without discontinuities. H_S is a Heaviside function across discontinuity surface S defined as

$$H_S(\boldsymbol{x}) = \begin{cases} 1 & \text{if } \boldsymbol{x} \in \Omega_+ \\ 0 & \text{if } \boldsymbol{x} \in \Omega_- \end{cases} \tag{2}$$

where $\boldsymbol{x}$ is the global coordinates of a given material point on Ω. Material points that are on one side of the surface S, in the subdomain Ω_+ will be termed as active points, and the rest as inactive, Fig. 1a. The vector $\boldsymbol{w}$ is the displacement jump vector across the discontinuity surface S. Equation 1 can be modified by adding and subtracting a jump-related term as in [Foster et al., 2007], making it more convenient for later finite element implementation. The term is a product of the jump vector $\boldsymbol{w}$ by an arbitrary smooth function f^h. This function has zero values at material points on $\Omega_- \backslash \Omega_-^h$, and unity values at material points on $\Omega_+ \backslash \Omega_+^h$ with a smooth transition between these points. Ω_+^h represents active part of the element bulk for elements intersected by the discontinuity, and Ω_-^h indicates the inactive part. Superscript h corresponds to the finite element discretization of body Ω. Accordingly, for a given set of localized elements in a discretized body Ω^h, S_+^h consists of the corresponding nodes and element sides not intersected by the discontinuity surface and connecting those nodes located on the active side, and S_-^h on the inactive side, Fig. 1b. The function f^h, in a finite element approximation, is characterized by element nodal values of unity and zero (conforming to the Heaviside function), for active and inactive parts, respectively, see Fig. 2. The displacement
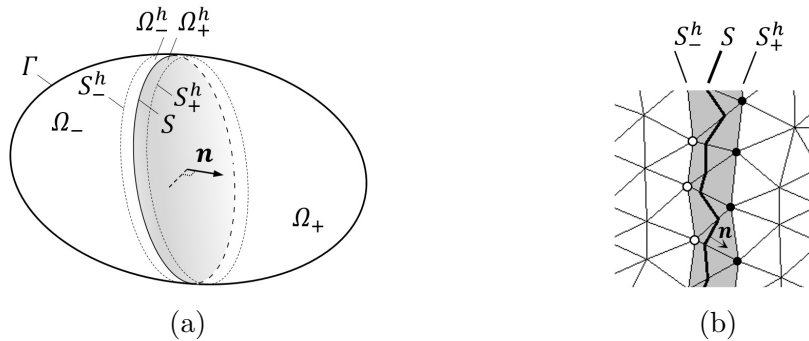

Figure 1: (a) Body Ω with displacement jumps added across a discontinuity surface S. $\Omega \backslash S$ is divided into active and inactive parts (Ω_+ and Ω_-, respectively), (b) S_+^h and S_-^h for a given set of localized elements (highlighted in gray); black circles indicate active nodes and white-filled circles represent inactive ones.

is then reformulated as

$$\boldsymbol{u} = \bar{\boldsymbol{u}} + f^h \boldsymbol{w} + H_S \boldsymbol{w} - f^h \boldsymbol{w}. \tag{3}$$

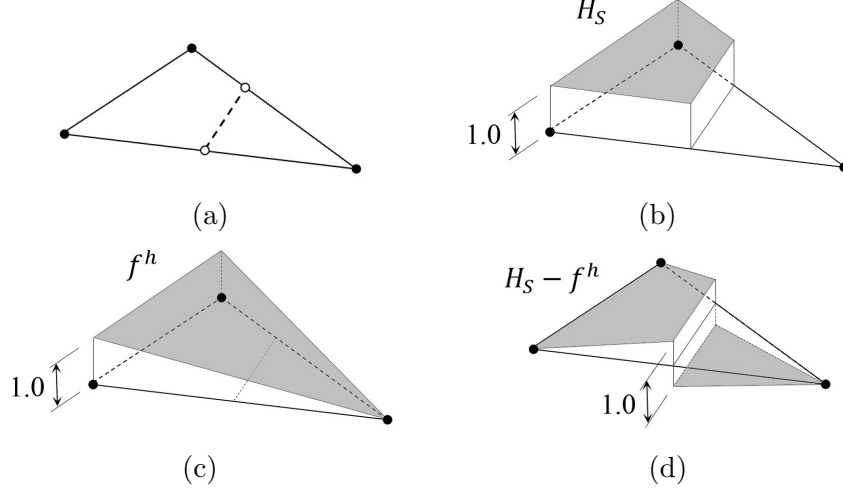Taking an appropriate form of f^h , e.g., sum of shape functions of the active nodes for a

Figure 2: (a) Constant stain triangular (CST) element showing a potential discontinuity surface (dashed line), (b) the Heaviside function H_S, (c) arbitrary smooth function f^h, (d) $H_S - f^h$.

given finite element, makes the first two terms of the right-hand side of Eq. 3 conform to the standard finite element shape functions. Hence, rewriting the equation gives

$$\boldsymbol{u} = \tilde{\boldsymbol{u}} + \left(H_S - f^h \right) \boldsymbol{w} \tag{4}$$

where $\tilde{\boldsymbol{u}}$ can be referred to as the conforming part of the displacement, see Fig. 3, and the last term of Eq. 4 represents the enhanced part.

The symmetric gradient of the displacement field, considering spatially constant jumps in each element, results in the strain field

$$\boldsymbol{\varepsilon} = \boldsymbol{\nabla}^s \boldsymbol{u} = \boldsymbol{\nabla}^s \tilde{\boldsymbol{u}} + \left[\boldsymbol{w} \otimes \left(\delta_S \boldsymbol{n} - \boldsymbol{\nabla} f^h \right) \right]^s \tag{5}$$

where $[\bullet]^s$ denotes the symmetric part of the tensor. The gradient of the step function H_S is $\delta_S \boldsymbol{n}$, where δ_S is the Dirac delta distribution across S, and $\boldsymbol{n}$ the normal to S pointing towards Ω_+. Accordingly, one may refer to the first term of the right-hand side of Eq. 5 as conforming strain, since it corresponds to the conforming displacement, and the last term as

strain enhancement as it corresponds to the displacement enhancement. For finite element implementation, strain terms can be rearranged and labeled as

$$\varepsilon = \underbrace{\boldsymbol{\nabla}^s \tilde{\boldsymbol{u}} - \left(\boldsymbol{w} \otimes \boldsymbol{\nabla} f^h\right)^s}_{\text{regular}} + \underbrace{\left(\boldsymbol{w} \otimes \boldsymbol{n}\right)^s \delta_S}_{\text{singular}} \tag{6}$$

where regular part corresponds to bounded strain terms, and singular part represents the unbounded term, inheriting its singularity from the Dirac delta's singularity across the discontinuity surface S. In the regular part, the jump effects are being subtracted from the conforming part, as conforming part had already those effects included. The singular part can be ignored in calculation of stress field since the stress in the continuum is considered to be only a function of the strain in that region. Thus, for linear elasticity,

$$\boldsymbol{\sigma} = \boldsymbol{C}^e : \boldsymbol{\varepsilon}^{\text{reg}} \tag{7}$$

where $\boldsymbol{C}^e$ is the fourth-order elastic modulus tensor, and superscript "reg" denotes the regular part. Computed stress is then in accordance with analyzing the balance of linear momentum, which implies traction continuity along discontinuity surface interfaces, without involving any unbounded term from within the surface, as in [Regueiro and Foster, 2011]. The traction continuity is given explicitly by

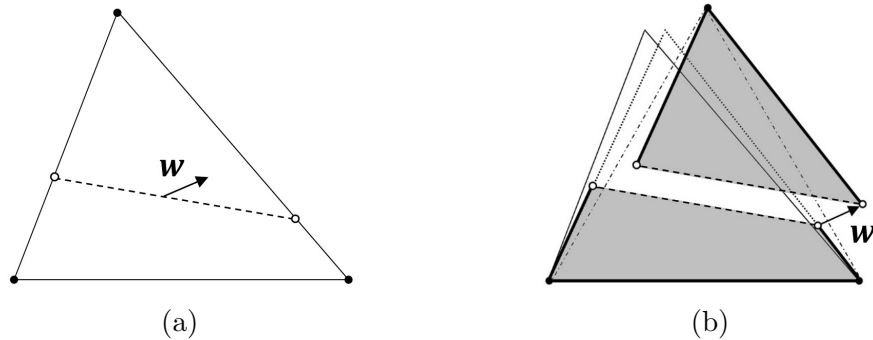$$\left(\boldsymbol{\sigma}_{S_+} - \boldsymbol{\sigma}_{S_-}\right) \cdot \boldsymbol{n} = \boldsymbol{0} \tag{8}$$

Figure 3: (a) Constant strain triangular (CST) element showing a potential discontinuity surface (dashed line) and the displacement jump vector $\boldsymbol{w}$, (b) a localized element with undeformed shape (fine lines), total deformed shape (bold lines), regular deformation (dotted lines), and conforming deformation (dash-dotted lines).

where $\boldsymbol{\sigma}_{S_+}$ is the stress tensor at a given material point adjacent to the discontinuity surface S on the active side, and $\boldsymbol{\sigma}_{S_-}$ on the inactive counterpart.

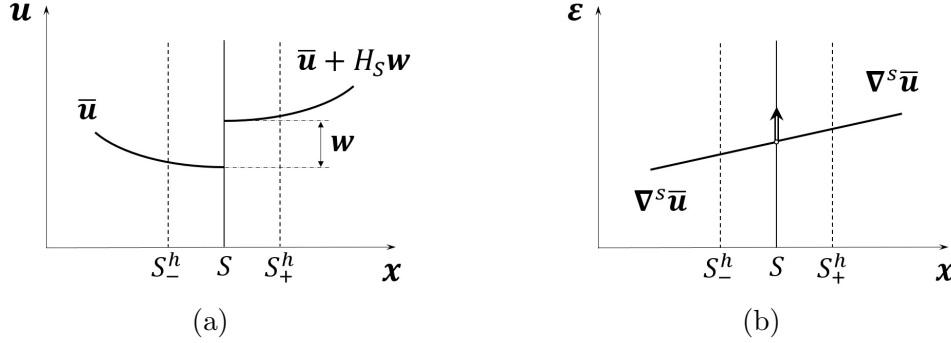Figure 4 illustrates a schematic description of the displacement and strain fields captured by Eqs. 4 and 6.

Figure 4: (a) Displacement field exhibiting jump along the discontinuity surface S, (b) strain field representing unbounded terms at the point of displacement discontinuity.

3. Traction-separation model

The constitutive response of a localized deformation is generally formulated in terms of a traction-separation model. This model will be suitable to a broader range of materials, in terms of ductile or brittle fracture, if it is able to capture the constitutive response not only for a fractured region, but also the process zone before any fracture is formed. This idea can be extended to the concept of weak and strong discontinuity mentioned earlier, i.e., a more general model is one that is capable of representing weakening characteristics of a localized region even without a displacement discontinuity. Such model can then play a significant role in a comprehensive analysis that spans the entire range of material behaviors from linear elastic to fully plastic. Hence, the two extremes of brittle fracture and plastic collapse [Anderson, 2005] along with the behaviors in between can be accounted for within one model provided that the model is equipped with a set of appropriate and accurate material parameters. The reader is referred to [Elices et al., 2002; Planas et al., 2003; De Borst, 2003] among others for further reviews and generalizations. Such a model, which can potentially raise numerical complexities, is beyond the scope of this work; instead, a

11

simple traction-separation model is adopted to provide a relatively simple framework for focusing on some of the numerical aspects of strain localization modeling. More advanced models can be found in [Camacho and Ortiz, 1996; Carol et al., 1997; Gálvez et al., 2002; Weed et al., 2015] among others.

3.1. Cohesive crack model

As a modification of the strip-yield model pioneered by Dugdale [Dugdale, 1960] and Barenblatt [Barenblatt, 1962], cohesive crack models were first adopted for concrete by Hillerborg and co-workers [Hillerborg et al., 1976]. These models were also initially termed as fictitious crack models, and later labeled as cohesive zone models, cohesive process zone models, and damage zone models [Hillerborg, 1991]. Cohesive crack models are proven to be an appropriate tool to model fracture formation in materials that experience nonlinearities due to pre-failure micro-cracking and having a linear stress-strain relation before any localized failure mechanism starts to dominate the overall constitutive response [Hillerborg, 1991]. Concrete is a good example of such materials, though the model has been shown to be applicable to a wide range of other materials as well, as shown in [Elices et al., 2002].

Cohesive crack models are well known to provide a formulation with a physical logic behind and within a simple framework [Cendón et al., 2000]. Tensile fracture in quasi-brittle and ductile materials with local mode I fracture dominating the overall medium response are problems where these models provide admissible results [Elices et al., 2002]. They estimate cohesive forces along surfaces where material particles are being pulled apart and cohesive strength is degrading. Therefore, they are able to describe the behavior of uncracked areas undergoing localized deformation. In this study, a cohesive crack model similar to the model used in the work of [Sancho et al., 2007] is adopted. The model allows for tangential as well as normal separation, and is a simple generalization to mixed mode fracture with the assumption that the traction vector is parallel to the displacement jump vector across the discontinuity interfaces.

The traction-separation relationship is defined as

$$\boldsymbol{t} = \frac{f(\tilde{w})}{\tilde{w}}\boldsymbol{w} \tag{9}$$
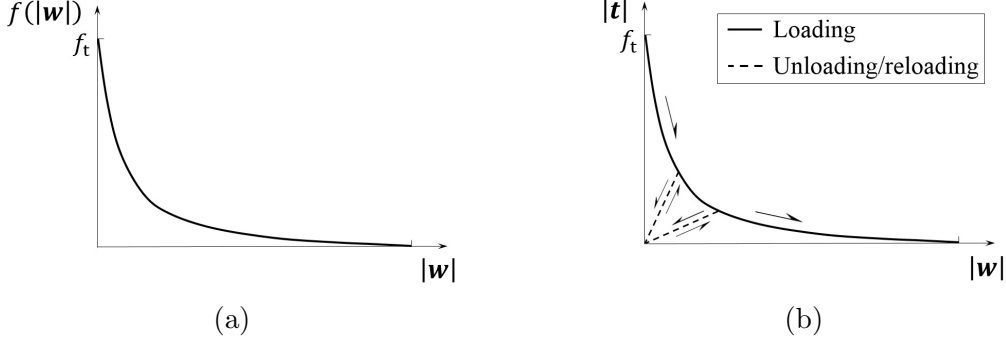
Figure 5: (a) Exponential softening curve, (b) traction-separation curve.

where $\boldsymbol{t}$ is the traction vector and $\boldsymbol{w}$ represents the displacement jump vector. The quantity $\tilde{w}$ is the historical maximum of the magnitude of the displacement jump vector throughout the simulation defined as

$$\tilde{w} = \max_t \left(|\boldsymbol{w}(t)| \right) = \max_t \left(\sqrt{w_n^2 + w_s^2} \right). \tag{10}$$

The quantities w_n and w_s are normal and sliding components of the displacement jump vector, respectively. The softening function $f(\tilde{w})$ in this study is defined as an exponential function as

$$f(\tilde{w}) = f_t \exp \left(-\frac{\tilde{w} f_t}{G_F} \right) \tag{11}$$

where the tensile strength f_t is the stress at which the crack forms and starts to open, and the cohesive fracture energy G_F is the external energy required to form and fully break a unit surface area of the cohesive crack. Typically, cohesive crack models, including the one used here, determine the work of separation (fracture energy) required for the complete formation of a discontinuity surface. This value corresponds to the area under the softening curve, Fig. 5a, as

$$G_F = \int_0^{w_c} f(|\boldsymbol{w}|) \, \mathrm{d}w \tag{12}$$

where w_c is the critical crack displacement, which corresponds to the state that the discontinuity interfaces are fully separated and cohesive strength is zero [Elices et al., 2002]. Theoretically, in this softening function, cohesion reaches zero at $\tilde{w} = \infty$, but practically the cohesive force can be made to reach a very small value relatively quickly. Figure 5a

13

represents a schematic curve for the exponential softening function at which f_t corresponds to the maximum cohesive strength. Figure 5b depicts the traction-separation curve for a sample softening function. During unloading the traction decreases towards the origin in a linear fashion. On reloading the traction follows the same linear path until $w = \tilde{w}$, where it begins again to soften.

Remark 1. *A connection can be made between the cohesive crack model parameters and the concept of weak/strong discontinuity, roughly speaking. This analogy will be more reasonable and accurate if the given cohesive model is complex enough to effectively take into account the constitutive response qualities of fracture process zone or the localization phenomenon is more characterized by strong discontinuity features. In that case, the tensile strength f_t can be considered as the stress at which the localized deformation initiates and hence the discontinuity starts to form. The cohesive fracture energy G_F is then the energy required for a unit surface area of weak discontinuity at initiation stage to be fully fractured. This energy is basically consumed in the straining of the localized region and the formation of the two new fracture surfaces.*

4. Finite element implementation

The finite element implementation follows the approach of assumed enhanced strain method as in [Simo et al., 1993; Borja and Regueiro, 2001; Foster et al., 2007] among others. The reader is referred to those works for detailed mathematical formulations and derivations. The primary steps include the development of the weak form of the governing equilibrium equations and the discretized variational equations (the Galerkin form), which are not derived here to avoid repetition. Provided below are the relevant finite element matrix equations developed for quasi-static problems under the assumption of infinitesimal deformation. All equations are in matrix form except for Eqs. 14 and 15. Matrix forms are adopted for computational efficiency.

4.1. The governing equilibrium finite element matrix equations

The standard residual statement for balance of linear momentum of element e (with domain Ω_e^h and boundary Γ_e^h) for the quasi-static small strain kinematics takes the matrix

form of

$$\boldsymbol{R}_e = \int_{\Omega_e^h} \boldsymbol{B}_e^{\mathrm{T}} \cdot \{\boldsymbol{\sigma}_e^h\} \; \mathrm{d}\Omega - \int_{\Omega_e^h} \boldsymbol{N}_e^{\mathrm{T}} \cdot \boldsymbol{b} \; \mathrm{d}\Omega - \int_{\Gamma_{e\,\boldsymbol{t}}^h} \boldsymbol{N}_e^{\mathrm{T}} \cdot \boldsymbol{t}_e^h \; \mathrm{d}\Gamma = \boldsymbol{0} \qquad (13)$$

where $\boldsymbol{B}_e$ is the standard finite element strain-displacement matrix, $\{\boldsymbol{\sigma}_e^h\}$, the element stress in vector form, $\boldsymbol{N}_e$, the standard finite element shape function matrix, $\boldsymbol{b}$, the prescribed body force vector, and $\boldsymbol{t}_e^h$ denotes the prescribed surface traction vector over the element boundary $\Gamma_{e\,\boldsymbol{t}}^h$. Equation 13 is valid for all elements; however, for the case of a localized element, an additional residual equation is needed to express the weak form for traction continuity on the discontinuity surface S. For a given localized element whose constitutive response is characterized by cohesive crack model, this traction vector is formed using both the stress tensor evaluated at integration points within the bulk of the element and projected onto the discontinuity surface, and the element-level traction-separation relationship imposed on S. In the case of the linear triangular element used here, the stress is constant within an element and therefore the projection is trivial. From Eq. 6, we can write the bulk stress of a localized element as a function of regular strain, ignoring the singular part similar to Eq. 7 as

$$\boldsymbol{\sigma}_e^h = \boldsymbol{C}^e : \boldsymbol{\varepsilon}_e^{h\,\mathrm{reg}} = \boldsymbol{C}^e : \left[\boldsymbol{\nabla}^s \tilde{\boldsymbol{u}}_e - \left(\boldsymbol{w}_e \otimes \boldsymbol{\nabla} f_e^h \right)^s \right] \qquad (14)$$

where $\boldsymbol{C}^e$ represents the fourth-order elastic modulus tensor, and superscript "reg" denotes the regular strain. The corresponding traction vector $\boldsymbol{t}_e$ on the discontinuity surface can then be written as

$$\boldsymbol{t}_e = \boldsymbol{n}_e \cdot \boldsymbol{\sigma}_e^h = \boldsymbol{n}_e \cdot \boldsymbol{C}^e : \boldsymbol{\varepsilon}_e^{h\,\mathrm{reg}} = \boldsymbol{n}_e \cdot \left[\boldsymbol{C}^e : \boldsymbol{\varepsilon}_e^{h\,\mathrm{conf}} - \boldsymbol{C}^e : \left(\boldsymbol{w}_e \otimes \boldsymbol{\nabla} f_e^h \right)^s \right] \qquad (15)$$

where $\boldsymbol{n}$ is the unit normal to the discontinuity surface S pointing towards Ω_+, Fig. 1, and superscript "conf" represents the conforming strain. On the other hand, Eq. 9 gives the other estimation for traction vector explicitly as a function of displacement jump vector $\boldsymbol{w}$. Traction continuity, using Eqs. 9 and 15, in matrix form then implies

$$\left[\frac{f\left(\tilde{w}_e \right)}{\tilde{w}_e} \right] \boldsymbol{w}_e = [\boldsymbol{n}_e] \cdot [\boldsymbol{C}^e] \cdot \left\{ \boldsymbol{\varepsilon}_e^{h\,\mathrm{conf}} \right\} - \left([\boldsymbol{n}_e] \cdot [\boldsymbol{C}^e] \cdot \left[\boldsymbol{\nabla} f_e^h \right] \right) \cdot \boldsymbol{w}_e \qquad (16)$$

15

where different notations in the form of $[\boldsymbol{C}^e]$ and $\left\{\boldsymbol{\varepsilon}_e^{h\,\mathrm{conf}}\right\}$ are used to represent the matrix and vector forms of the tensors $\boldsymbol{C}^e$ and $\boldsymbol{\varepsilon}_e^{h\,\mathrm{conf}}$, respectively. The vector $\boldsymbol{n}_e$ in Eq. 15 is also adjusted as $[\boldsymbol{n}_e]$ in Eq. 16 to conform to the matrix form of the equation. More details are provided in Appendix A.1. Equation 16 gives the residual expression for balance on the discontinuity surface S as

$$\boldsymbol{r}_e = \left(\frac{f(\tilde{w}_e)}{\tilde{w}_e} \mathbf{1} + [\boldsymbol{n}_e] \cdot [\boldsymbol{C}^e] \cdot \left[\boldsymbol{\nabla} f_e^h \right] \right) \cdot \boldsymbol{w}_e - [\boldsymbol{n}_e] \cdot [\boldsymbol{C}^e] \cdot \left\{ \boldsymbol{\varepsilon}_e^{h\,\mathrm{conf}} \right\} = \mathbf{0} \qquad (17)$$

where $\mathbf{1}$ is a 2-by-2 identity matrix, and those terms involving $\boldsymbol{w}$ are factored out and grouped together. Equation 17 is a nonlinear balance equation, arising from the strong discontinuity, which can be solved for the displacement jump vector $\boldsymbol{w}_e$ using an element-level Newton-Raphson iterative solution algorithm.

4.2. Consistent stiffness matrix

A consistent stiffness matrix is needed for each localized element to solve for the global Newton-Raphson iteration. To form a consistent stiffness matrix for a given localized element with a known displacement jump vector, Eqs. 13 and 17 must be met. Linearization of these equations by taking a variation for solution by the Newton-Raphson method, following the procedure in [Borja and Regueiro, 2001], results in

$$\delta \boldsymbol{R}_e = \boldsymbol{K}_e^{dd} \cdot \delta \boldsymbol{d}_e + \boldsymbol{K}_e^{dw} \cdot \delta \boldsymbol{w}_e \qquad (18)$$

$$\delta \boldsymbol{r}_e = \boldsymbol{K}_e^{wd} \cdot \delta \boldsymbol{d}_e + \boldsymbol{K}_e^{ww} \cdot \delta \boldsymbol{w}_e \qquad (19)$$

where

$$\boldsymbol{K}_e^{dd} = \frac{\partial \boldsymbol{R}_e}{\partial \boldsymbol{d}_e} \qquad (20)$$

$$\boldsymbol{K}_e^{dw} = \frac{\partial \boldsymbol{R}_e}{\partial \boldsymbol{w}_e} \qquad (21)$$

$$\boldsymbol{K}_e^{wd} = \frac{\partial \boldsymbol{r}_e}{\partial \boldsymbol{d}_e} \qquad (22)$$

$$\boldsymbol{K}_e^{ww} = \frac{\partial \boldsymbol{r}_e}{\partial \boldsymbol{w}_e}. \qquad (23)$$

Equation 20 is simply the standard element stiffness matrix as

$$\boldsymbol{K}_e^{dd} = \int_{\Omega_e^h} \boldsymbol{B}_e{}^{\mathrm{T}} \cdot [\boldsymbol{C}^e] \cdot \boldsymbol{B}_e \ \mathrm{d}\Omega \tag{24}$$

and subsequent quantities are calculated by taking derivatives, which are given explicitly in matrix form by

$$\boldsymbol{K}_e^{dw} = -\int_{\Omega_e^h} \boldsymbol{B}_e{}^{\mathrm{T}} \cdot [\boldsymbol{C}^e] \cdot \left[\boldsymbol{\nabla} f_e^h\right] \ \mathrm{d}\Omega \tag{25}$$

$$\boldsymbol{K}_e^{wd} = -[\boldsymbol{n}_e] \cdot [\boldsymbol{C}^e] \cdot \boldsymbol{B}_e \tag{26}$$

$$\boldsymbol{K}_e^{ww} = \begin{cases} \frac{f(\tilde{w}_e)}{\tilde{w}_e}\mathbf{1} + [\boldsymbol{n}_e] \cdot [\boldsymbol{C}^e] \cdot \left[\boldsymbol{\nabla} f_e^h\right] - \left[\frac{f(\tilde{w}_e)\left(\frac{\tilde{w}_e f_t}{G_{\mathrm{F}}}+1\right)}{\tilde{w}_e^3}\right] \boldsymbol{w}_e \otimes \boldsymbol{w}_e & \text{if } |\boldsymbol{w}_e| > \tilde{w}_e \\[2mm] \frac{f(\tilde{w}_e)}{\tilde{w}_e}\mathbf{1} + [\boldsymbol{n}_e] \cdot [\boldsymbol{C}^e] \cdot \left[\boldsymbol{\nabla} f_e^h\right] & \text{if } |\boldsymbol{w}_e| \leq \tilde{w}_e. \end{cases} \tag{27}$$

The quantity $\tilde{w}_e$ is the historical maximum of the magnitude of the displacement jump vector of the localized element e throughout the simulation. The condition for Eq. 27 is checked at each element-level (local) Newton-Raphson iterating. The term $\boldsymbol{\nabla} f_e^h$ can be represented in Voigt notation as

$$\left[\boldsymbol{\nabla} f_e^h\right] = \begin{bmatrix} f_{e\ ,x}^h & 0 \\ 0 & f_{e\ ,y}^h \\ f_{e\ ,y}^h & f_{e\ ,x}^h \end{bmatrix} \tag{28}$$

where $f_{e\ ,x}^h$ and $f_{e\ ,y}^h$ are summation of gradient of shape functions for the active nodes of element e in x and y directions, respectively.

Since the displacement jump vector $\boldsymbol{w}_e$ is assumed to be discontinuous across elements (an element-level quantity with no effects on neighbor elements), it can be statically condensed out of the equations at that level. The resulting condensed element stiffness matrix following the procedure in [Foster et al., 2007] then reads

$$\boldsymbol{K}_e = \boldsymbol{K}_e^{dd} - \boldsymbol{K}_e^{dw} \cdot \boldsymbol{K}_e^{ww-1} \cdot \boldsymbol{K}_e^{wd}. \tag{29}$$

Considering $\boldsymbol{K}_e^{dd}$ as the standard stiffness matrix for a non-localized element, Eq. 29 reveals how stiffness is modified for a localized element by a softening component $\boldsymbol{K}_e^{dw} \cdot \boldsymbol{K}_e^{ww-1} \cdot \boldsymbol{K}_e^{wd}$ that is characterized primarily by the introduced jump along the discontinuity surface S. As a

result of this condensation procedure, nodal displacements are the only remaining unknowns to solve for at global-level finite element approximation. By using this strategy, the assumed enhanced strain method can be incorporated quite easily into any available finite element algorithm with few further global-level modifications.

Remark 2. *Given a localized element, Eq. 16 reveals the constitutive response softening nature of the weakening element. The right-hand side of the equation is from the kinematics of the assumed enhanced strain method within finite element framework. The left side, originated from the exponential cohesive crack model, is the key term in characterizing the material softening characteristics of a localized element. This term can be replaced by more sophisticated traction-separation relationships, material plasticity- or damage-like models (generally any macroscopic level displacement-softening model) to provide a rheologically more accurate and suitable solution for a strain localization problem at hand with a specific material type.*

5. Tracking the evolution of localized deformation

The evolution of localized deformation, either with an instantaneous appearance, e.g., in homogeneous strain localization problems or in the form of a relatively gradual propagation of the localized region, may require an auxiliary tracking algorithm to trace the discontinuity path as it evolves. Employing such an algorithm becomes a necessity within the class of inter-element discontinuities in finite elements.

The classical approach for such tracking purpose lies on detecting the most critical element (based on the criteria used to find the initiation of localization at each material point) and propagating the localization band from that critical element (root element) and tracing the band from element to element. This method in which the discontinuity surface evolution is traced element by element is referred to as the local tracking. One algorithm for local tracking is outlined in more detail in [Foster et al., 2007]. An alternative approach, which is developed relatively recently, is referred to as the global tracking. In this approach, all potential discontinuity surfaces are detected at once. Then, based on single- or multi-band nature of the localization problem, the active surface or surfaces are identified [Oliver et al., 2002].

5.1. Local tracking

Conducting a tracking algorithm requires identifying the set of localized elements. Such a set, at each point of the simulation, consists of the elements that can be potentially crossed by a discontinuity surface. The identification process is considered as a preliminary step that includes checking the whole discretized body to find elements that pass the criteria for the onset of localization. If at least one localized element is found, the tracking starts. The next step then is to find the most critical element (in this case the element with the largest maximum tensile stress) among the set of localized elements. If there is only one localized element detected, that element will be the critical one. This search process identifies the first root element (seed element) from which the first discontinuity surface initiates.

The local tracking algorithm needs two essential ingredients for a given localized element to propagate the band. The spatial coordinates of one material point on the discontinuity surface, either within the domain of the localized element $\Omega^h_{e,\,\text{loc}}$ or on its boundary $\Gamma^h_{e,\,\text{loc}}$ (element edges) are required to locate the band. This point is chosen to be the centroid for the root element, and the intersection of an element edge with the approaching discontinuity surface from an adjacent element for other elements. The second piece of information comes from the localization orientation. The orientation follows from the localization criterion, in this study, the direction orthogonal to the maximum principal stress.

As depicted in Fig. 1b, the element edges crossed by the discontinuity surfaces are those having an active node on one side, and an inactive one on the other side. The need for determining the status (in terms of being active or inactive) for the nodes of elements crossed by the discontinuity surfaces has two aspects. First, it is used by the tracking algorithm to identify the element edges that will be crossed. Second, it affects the kinematics of those intersected elements by embedding different localization modes into displacement and strain formulations using f^h (sum of shape functions of the active nodes for a given finite element) and ∇f^h, via Eqs. 4 and 6. The determination is subsequently needed in forming ∇f^h_e to express the residual expression for balance on the discontinuity surface S, Eq. 17, for a localized element e. This determination can be performed by the use of one material point on the discontinuity surface and the normal to the surface pointing towards the active side of the element.

Using the aforementioned information as input data, the local tracking algorithm traces the first discontinuity surface. If a multi-surface localization problem is of interest, the algorithm continues the search process to detect other surfaces. Searching for root elements, except for the first one, should be performed within the set of untraced localized elements for a given tracking procedure. This prevents the formation of trivial bands located at the position of previously traced surfaces. Box 1 represents a rough algorithmic summary of the local tracking algorithm. The reader is referred to [Foster et al., 2007] for detailed formulations and algorithmic implementation procedure.

Box 1: Summary of the local tracking algorithm.

Step 1: Check the onset of localization for all elements. If no localized element is detected, then exit.

Step 2: If the band has not been traced yet, find the root element with the largest maximum tensile stress among the set of localized elements. Otherwise, go to *Step 4*.

Step 3: Propagate the band from the centroid of the root element to get its intersection with the element edges.

Step 4: Check the untraced elements at the end of the existing band for localization. If localized, propagate the band. (The propagation continues until either the untraced adjacent elements of all bands are not localized or boundary Γ^h is reached.)

Step 5: If the algorithm is carried out at the end of a time step, fix localization orientation for elements crossed by the discontinuity surface(s).

Step 6: If allowing for multiple bands: If a new potential band has not been traced yet, find the root element with the largest maximum tensile stress among the set of untraced localized elements, and go to *Step 3*. Otherwise, go to *Step 4*. If single band is expected, then exit.

5.2. Stabilizing crack tip technique

5.2.1. Motivation

A stabilizing crack tip technique is proposed to fix incorrect discontinuity surface evolution in some strain localization problems, especially those with notched sides introduced on the boundary. One may observe such an issue by estimating localization orientation based upon maximum principal direction. The incorrect localization orientation, and subsequently
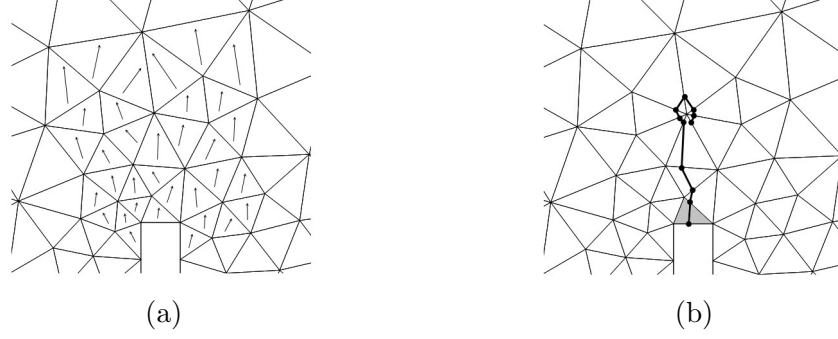
20

Figure 6: (a) Element-level localization orientations represented as inter-element vectors within the discretized body with a side notch introduced on its boundary, (b) returning pattern of surface evolution due to an inaccurate estimation of principal directions.

the inaccurate surface evolution, which typically occurs at a crack tip zone is considered to be a result of the bad estimation of principal directions due to high stress gradients at the tip area [Sancho et al., 2007]. Furthermore, using the maximum principal stress criterion means making the (simplifying) assumption of local mode I fracture being dominant at the crack tip zone. Inaccurate crack evolution can then occur when mode II fracture becomes significant in case of a mixed mode loading or unstable crack growth [Cendón et al., 2000].

To illustrate the issue, one may consider all potential discontinuity surfaces within a body, Fig. 6a. Adjacent potential surfaces are usually similar in orientation, having a gradual change in orientation throughout the body. These roughly parallel lines, along with the inaccurate principal directions estimation mentioned earlier, results in a returning pattern in surface propagation. As sketched in Fig. 6b, one critical surface starts from the root element (highlighted in gray), then jumps to an adjacent potential surface and returns.

5.2.2. Implementation

The steps needed to implement the stabilizing crack tip technique are summarized in Box 2. These steps can be embedded within *Step 4* of the main local tracking algorithm, Box 1. Figure 7 demonstrates a schematic representation of implementing the technique to improve the accuracy of surface evolution and avoiding a returning propagation pattern. The quantity ($\theta_{\mathrm{allowed}}$) is usually taken to be $\pi/2$ radians.
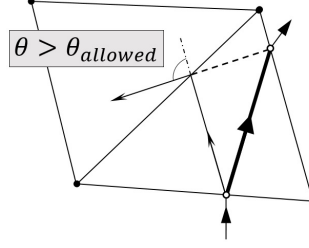
21

Figure 7: Stabilizing crack tip technique. Discontinuity surface (fine solid line) approaching two adjacent elements with surface orientation getting modified (bold solid line).

Box 2: Summary of the stabilizing crack tip technique implementation.

Step 1: Check surface orientation change as it evolves from a host element to an adjacent element, thin solid line in Fig. 7. If the change is greater than a prescribed allowable value ($\theta_{\mathrm{allowed}}$), perform stabilizing crack tip technique. Otherwise, go to *Step 5*.

Step 2: Propagate the surface towards the host element, instead of the adjacent element, using the localization orientation of the adjacent element (dashed line).

Step 3: Update the new surface orientation for the host element. In Fig. 7, bold solid line represents the updated surface path. The adjacent element remains untraced.

Step 4: Check the host element for localization at the new imposed direction. If localized, trace the element and go to *Step 5*. Otherwise, leave the host element as untraced, then exit. (The host element remains as a localized element for further tracking.)

Step 5: Continue surface propagation.

5.3. Global tracking

An essential part of a global tracking algorithm consists of a solution of a steady-state heat conduction-like problem with no internal heat source and null heat flux input, Fig. 8. The boundary value problem to be solved (with domain Ω and boundary $\Gamma = \Gamma_{\boldsymbol{q}} \cup \Gamma_T$) can
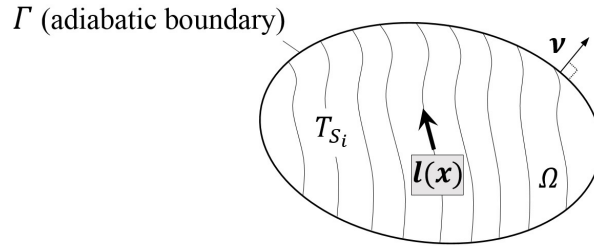
Figure 8: The steady-state heat conduction-like problem.

be represented as

Find $T(\boldsymbol{x})$, such that:

$$\boldsymbol{\nabla} \cdot \boldsymbol{q} = 0 \quad \text{in } \Omega \quad \text{(a)}$$

$$\boldsymbol{q} = -\boldsymbol{K} \cdot \boldsymbol{\nabla} T \quad \text{in } \Omega \quad \text{(b)}$$

$$\boldsymbol{q} \cdot \boldsymbol{\nu} = 0 \quad \text{on } \Gamma_{\boldsymbol{q}} \quad \text{(c)}$$

$$T = T^* \quad \text{on } \Gamma_T \quad \text{(d)} \tag{30}$$

where $T(\boldsymbol{x})$ is the temperature of a material point represented by its spatial coordinates $\boldsymbol{x}$; hence, the solution of the boundary value problem above provides the temperature field throughout the domain Ω. The term $\boldsymbol{q}$ is the conduction flux-like vector, $\boldsymbol{\nu}$, the outward normal to the boundary Γ, T^*, the prescribed temperature over the boundary Γ_T, and $\boldsymbol{K}$ denotes a material point dependent anisotropic thermal conductivity tensor which is given explicitly by

$$\boldsymbol{K}\left(\boldsymbol{l}(\boldsymbol{x})\right) = [\boldsymbol{l} \otimes \boldsymbol{l}]. \tag{31}$$

The vector $\boldsymbol{l}(\boldsymbol{x})$ represents the discontinuity surface orientation at material point $\boldsymbol{x}$ (following from the localization criterion, i.e., the direction orthogonal to the maximum principal stress) in the form of a unit vector signaling the direction of the localization evolution. In order to overcome the singularity of the conductivity tensor, an isotropic algorithmic component of the conductivity, ϵ, is added. Therefore, the thermal conductivity tensor gets modified as

$$\boldsymbol{K}\left(\boldsymbol{l}(\boldsymbol{x})\right) = [\boldsymbol{l} \otimes \boldsymbol{l}] + \epsilon \boldsymbol{1}. \tag{32}$$

where $\boldsymbol{1}$ is the identity tensor. The reader is referred to [Oliver and Huespe, 2004] for detailed formulations, derivations, and discretized equations in a finite element setting.

In a finite element context, the solution of the heat conduction-like problem above provides the nodal temperature values of the discretized body. Now, the potential discontinuity surfaces denoted by S_i can be considered as isothermal lines of the heat conduction problem, i.e., sets of material points with each set having an identical temperature. These disconti-

nuity surfaces can be represented as

$$S_i := \{ \boldsymbol{x} \in \Omega; \ T_{\boldsymbol{x}} = T_{S_i} \} . \tag{33}$$

After identifying the potential surfaces, the next step then is to find the most critical element (the element with the largest maximum tensile stress) among the set of localized elements. This search process identifies the first root element (seed element), and the isothermal line passing through this element reveals the first discontinuity surface. The temperature of the isothermal line is simply the average nodal temperature of the root element. This choice is in accordance with taking the centroid of the root element as the initiation point of the discontinuity surface in a local tracking algorithm. If a multi-surface localization problem is of interest, the algorithm continues the search process to detect other surfaces. Searching for root elements, except for the first one, should be performed within the set of untraced localized elements for a given tracking procedure. This search continues until there are no more critical elements left within the body. Box 3 represents a summary of the global tracking algorithm. In order to increase computational efficiency, a simplified version of the global tracking algorithm was used throughout this study by avoiding the detection of all potential discontinuity surfaces based on the knowledge of the number of bands being formed. Such detection process is helpful in a multi-surface localization problem, but trivial for the simulations performed here. Therefore, time tables provided in Section 6 represent underestimated simulation times for the global tracking strategy compared to the general algorithm illustrated here in Box 3.

Determining the status (in terms of being active or inactive) for the nodes of elements crossed by the discontinuity surface within the global tracking algorithm may be carried out in a different way compared to the local tracking. The isothermal line temperature (the average nodal temperature of the root element) can be used for such purpose. Nodes having greater nodal temperatures than the isothermal line are termed as active, and others as inactive, or vice versa depending on the direction of the unit normal to the surface.

Box 3: Summary of the global tracking algorithm.

Step 1: Check the onset of localization for all elements. If no localized element is detected, then exit.

Step 2: Solve the steady-state heat conduction-like problem for the discretized body Ω^h.

Step 3: Identify the sets of potential discontinuity surfaces S_i.

Step 4: If the band has not been detected yet, find the root element with the largest maximum tensile stress among the set of localized elements.

Step 5: Determine the discontinuity surface, which would be in accordance with the isothermal line passing through the root element.

Step 6: If the algorithm is carried out at the end of a time step, fix nodal temperature for elements crossed by the discontinuity surface(s).

Step 7: If allowing for multiple bands: If a new potential band has not been detected yet, find the root element with the largest maximum tensile stress among the set of untraced localized elements, and go to *Step 5*. Otherwise, go to *Step 5* without searching for the root element. If single band is expected, then exit.

Remark 3. *The local and global tracking strategies have differences in implementation and performance. One advantage factor can be the information about potential discontinuity surfaces that each approach is equipped with at the time of tracking an active surface. The local tracking has no information on those still untraced surfaces, while the global tracking detects all potential surfaces before starting to identify the active ones. This key difference gives the global tracking approach a superior performance in multi-surface localization problems. One may also find the global tracking strategy simpler to implement for three-dimensional problems.*

6. Numerical simulations

In this section, some numerical simulations are presented in order to investigate the performance of the two updating schedules for tracking the band propagation over time; either at the end of each time increment, or during each iteration within a given time increment. The numerical algorithm capturing the strain localization response, along with the band tracking strategies, are adopted to model the subsequent examples, which helps us, for each updating schedule, in:

- Examining robustness. To compare robustness, the ability of the algorithm to successfully arrive at a solution for a complete simulation is considered.

- Quantifying accuracy. This is measured in terms of inter-element spatial location and orientation of localization surface paths, along with comparing the force-displacement curves for each updating schedule.

- Evaluating simulation time. In addition to total simulation time, two aspects of the simulations are examined. One factor is the rate of convergence for a sequence of successive approximations for Newton-Raphson's iterative algorithm. Generally, a quadratic rate is expected as the method converges, since Newton-Raphson is used for numerical solution of governing equations. The other factor is the number of times a tracking subroutine is called within a given time step. Tables are provided that present the simulation time and computational cost (by implication) for different tracking strategies and updating schedules employed.

6.1. Stretching of a homogeneous block

The first simulation is a plane strain stretching of a rectangular block, as shown in Fig. 9a. The material is linear elastic and isotropic with Young's modulus $E = 5.5\text{E}+03$ MPa and Poisson's ratio $\nu = 0.25$. The parameters used to describe the exponential softening function, Eq. 11, are tensile strength $f_\text{t} = 5.0\text{E}+01$ MPa and fracture energy $G_\text{F} = 5.0\text{E}+01$ N/mm. A displacement-controlled approach is carried out by applying $d = 0.01$ m upward prescribed displacement on the top side of the specimen. The constraints are provided on the bottom side such that the strain field and hence the stress become homogeneous. The homogeneity holds throughout the elastic part of the simulation, until strain localization initiates.

Two types of meshing have been developed using a standard constant strain triangle (CST) finite element: a 36-element coarse structured mesh, Fig. 9b, and a 70-element coarse unstructured mesh, Fig. 9c. The main local tracking algorithm, Box 1, was used for tracking purpose. The stabilizing crack tip technique was not required for this example. There are no side notches introduced in this simulation. Instead, seed elements are introduced to the tracking algorithm, since the problem is homogeneous. As a result, the block experiences
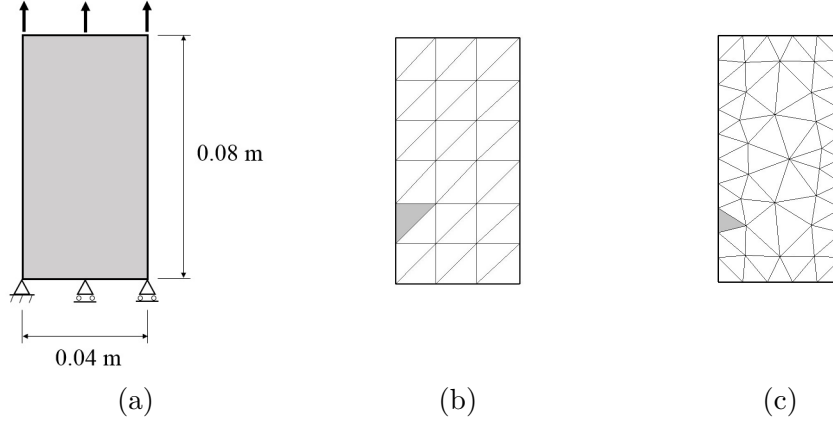
Figure 9: Stretching of a homogeneous block. (a) Dimensions, loading, and boundary conditions, (b) coarse structured finite element meshing, (c) coarse unstructured finite element meshing. Seed elements are shaded.

one localization band. Otherwise, all elements would surpass the tensile strength limit (the criterion for the onset of localization) at the same time due to homogeneity, creating multiple parallel bands within the body. Allowing only one band form is in accordance with what often happens in reality. Local imperfections, dislocations or micro cracks/voids commonly lead to one dominant discontinuity surface, letting the rest of the body unload elastically. The entire localization band forms instantly at the onset of localization without any band evolution throughout the simulation, since all elements localize at the same time. Seed element selection for an individual band is of no significance within the corresponding set of localized elements forming that band, i.e., choosing any of those localized elements as the root element results in a similar localization path. This property typically does not hold in a non-homogeneous problem.

The discontinuity surface paths and the deformed finite element meshes with vertical displacement distribution are illustrated in Figs. 10 and 11 for coarse structured and coarse unstructured mesh types, respectively. Across this section, the discontinuity surface paths, which are illustrated by dashed lines, only represent those localized elements that are in the loading phase, i.e., the unloading elements are not shown. The two cases have similar seed element elevations. The softening response is captured throughout a row of localized elements forming a horizontal strain localization band. This is the place where most of the block stretching is developed throughout the body.
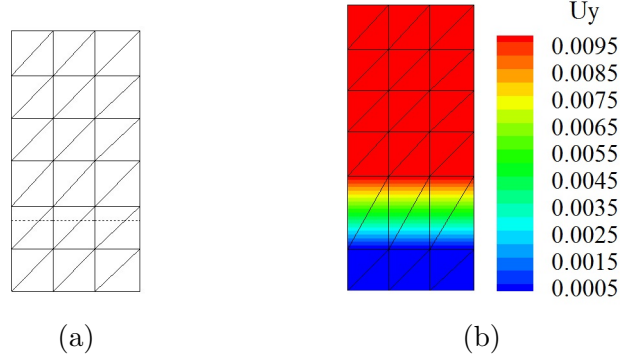
27

Figure 10: Stretching of a homogeneous block. Structured mesh, (a) dashed line represents the discontinuity surface path (only for elements in the loading phase), (b) deformed finite element mesh along with vertical displacement distribution.
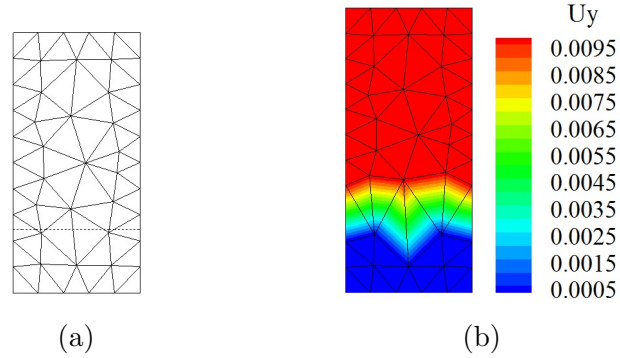

Figure 11: Stretching of a homogeneous block. Unstructured mesh, (a) dashed line represents the discontinuity surface path (only for elements in the loading phase), (b) deformed finite element mesh along with vertical displacement distribution.

Both simulations experience elastic behavior at the first stage of the process, while material failure occurs after some prescribed tensile strength is reached. Figures 12 and 13 provide the graphs for reaction forces versus imposed displacement for the unstructured meshing with the local tracking algorithm for 50 and 100 steps, respectively. The graph patterns for structured meshing and the global tracking algorithm are similar. Each figure compares the two cases of performing updating at the end of each time increment and within iterations in a given time increment. In both graphs, the former case gives a higher peak reaction force, which is an inaccurate estimation. This inaccuracy comes from the fact that updating is performed at the end of the step. Therefore, the localization initiation is delayed until the end of the time increment, whereas an earlier detection and softening occurs while performing the updating within iterations. This difference in peak reaction forces becomes smaller as time step size is refined, as shown in Fig. 13. For this example, which is considered
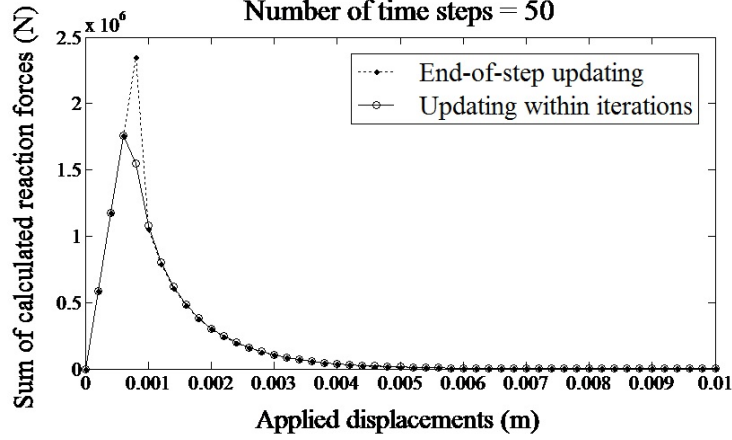
Figure 12: Stretching of a homogeneous block. Force-displacement graph for the unstructured mesh with the local tracking algorithm using 50 time steps for the two cases of performing end-of-step updating and updating within iterations.
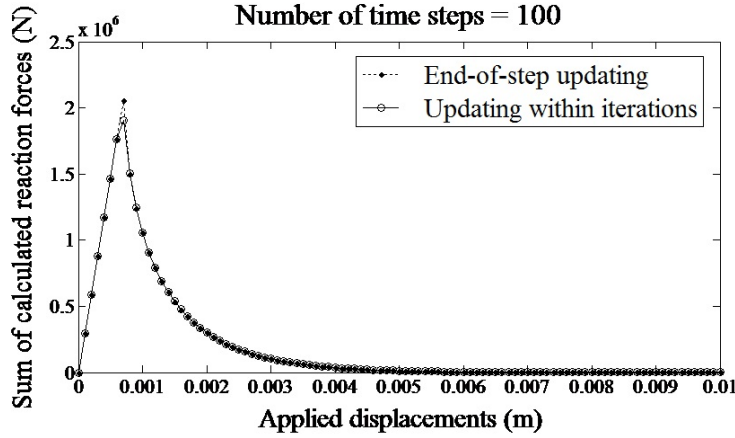

Figure 13: Stretching of a homogeneous block. Force-displacement graph for the unstructured mesh with the local tracking algorithm using 100 time steps for the two cases of performing end-of-step updating and updating within iterations.

as a homogeneous problem with instantaneous band propagation, the difference in estimated reaction forces appears only at the time that localization initiates (which also corresponds to the time that the entire band forms). The two force-displacement curves agree very closely both before and afterwards. Both updating schedules reveal identical localization surface paths in terms of inter-element spatial location and orientation.

In the homogeneous problem, both updating schedules complete the simulation without trouble. Hence, there are no robustness issues. Both band tracking algorithms produce identical results in this case as well.

Table 1 provides the simulation time for the adopted tracking strategies and updating

29

Table 1: Stretching of a homogeneous block. Simulation time for different tracking strategies and updating schedules using 50 time steps.

Mesh type	Tracking strategy	Updating schedule	Simulation time (sec.)
36-element structured mesh	Local tracking	End of step	86.07
		Within iterations	107.88
	Global tracking	End of step	84.26
		Within iterations	107.02
70-element unstructured mesh	Local tracking	End of step	250.49
		Within iterations	313.55
	Global tracking	End of step	242.23
		Within iterations	312.98

schedules. It takes relatively more time and computational cost when updating is carried out within the iterations, as expected. The tracking subroutine is called for every single iteration for updating within iterations while end-of-step updating calls the tracking subroutine only once; at the end of the step. Not much difference is observed comparing the local and global tracking strategies. Another factor affecting the simulation time is the rate of convergence. A faster convergence rate than quadratic was observed for performing updating at the end of each time step. However, for the case of performing updating within iterations, a slower rate than quadratic occurred. This slower convergence is observed only at the step where localization starts. After the localization initiates and the band forms, the set of localized elements remains identical for the two cases (without further band evolution), and quadratic convergence is then recovered. Embedding the set of softening elements within the global-level governing equations during the iterative solution is considered as the reason for such a relatively slower rate in converging.

Therefore, investigating the simulation time for the two updating schedules shows two causes for an increased computational cost of updating within iterations: one factor is the additional computations arising from the extra number of times that the tracking subroutine is called, and the other corresponds to the slower rate of convergence for a given evolving localization that results in additional iterations before a converged solution is reached.

6.2. Double-edge notched specimen under tension

The second example consists of a plane stress double-edge notched specimen under tension. Two cases are considered; notch offset values of 5 mm and 15 mm, as shown in Figs.
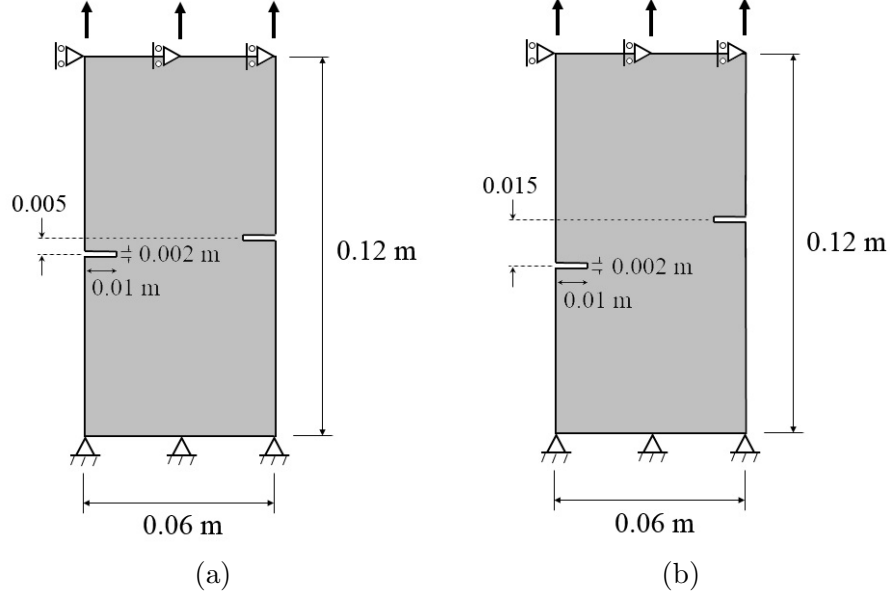
Figure 14: Double-edge notched specimen under tension. Dimensions, loading, and boundary conditions, (a) 5-mm notch offset, (b) 15-mm notch offset.

14a and 14b. These examples follow the simulations provided in [Alfaiate et al., 2002], based on experimental data from [Shi et al., 2005]. The offset values are measured in vertical direction and symmetric with respect to a horizontal axis passing through the center of the specimen. The material is linear elastic and isotropic with Young's modulus $E = 2.4\mathrm{E}{+}04$ MPa and Poisson's ratio $\nu = 0.2$. The parameters used to describe the exponential softening function, Eq. 11, are tensile strength $f_\mathrm{t} = 2.0$ MPa and fracture energy $G_\mathrm{F} = 5.9\mathrm{E}{-}02$ N/mm. The model has a thickness of 10 mm. A displacement-controlled approach is carried out by applying $d = 0.2$ mm upward prescribed displacement on the top side of the specimen.

6.2.1. Notch offset value of 5 mm

The model is discretized using a standard constant strain triangle (CST) finite element. The coarse unstructured meshing with blunt notch tips is developed using 198 elements, as shown in Fig. 15. The root elements are detected automatically by the tracking algorithm based on the most critical status of elements, i.e., the element having the largest maximum principal stress. This is in accordance with what typically happens in reality, where no manual imperfections are embedded at notch tip areas. The main local tracking algorithm, Box 1, was used for tracking purpose. The stabilizing crack tip technique was not required
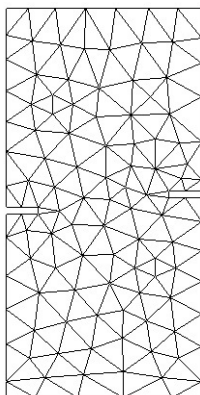
Figure 15: Double-edge notched specimen under tension (5-mm notch offset). Coarse unstructured meshing with automatic detection of the root elements.

for this simulation.

The simulation is carried out using 100 and 500 time steps. The discontinuity surface paths and the deformed finite element mesh with vertical displacement distribution are illustrated in Fig. 16 for the case of using 100 time steps. Figures 16a and 16c depict band paths for performing end-of-step updating and updating within iterations, respectively. For both cases, two separate bands start to evolve from the seed elements at the time of localization initiation. However, as the simulation continues, it reaches a point where one dominant band forms. Similar elevations of the root elements is the key parameter in capturing one dominant band for this simulation. For the case of end-of-step updating, the first band (lower one) evolves from the element located right by the notch tip at the left-hand side of the specimen until it reaches an element adjacent to the second root element on the right-hand side. The second band (upper one) then starts to evolve without any propagation

(a)   (b)   (c)   (d)
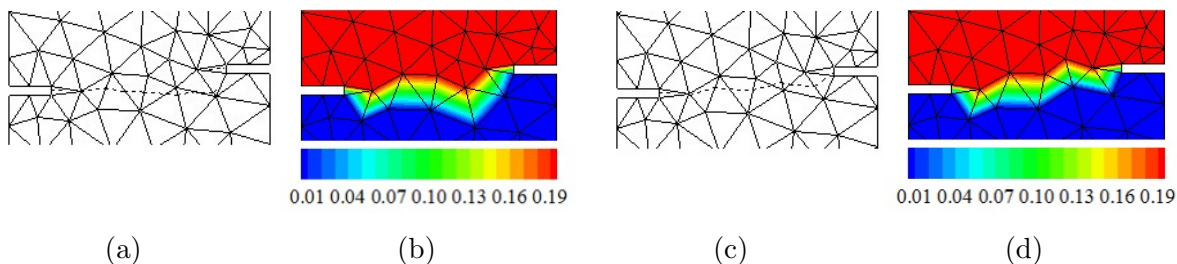
Figure 16: Double-edge notched specimen under tension (5-mm notch offset). Using 100 time steps and the local tracking algorithm, (a) dashed line represents the discontinuity surface paths (only for elements in the loading phase) for performing end-of-step updating, (b) deformed finite element mesh along with vertical displacement distribution, (c) surface path for performing updating within iterations, (d) deformed finite element mesh along with vertical displacement distribution.
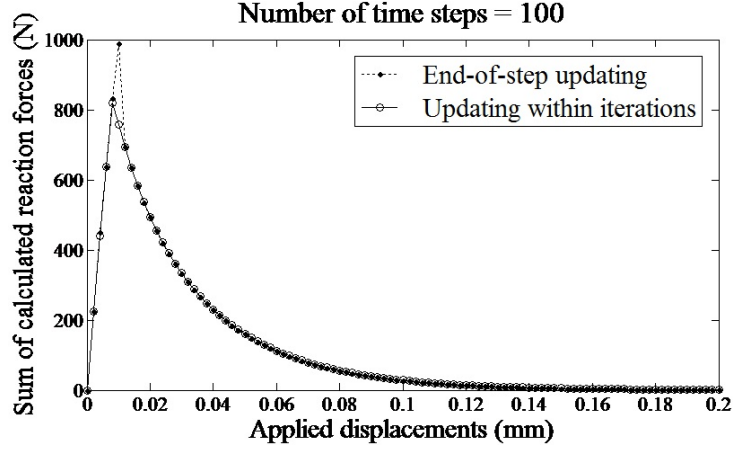
Figure 17: Double-edge notched specimen under tension (5-mm notch offset). Using 100 time steps, force-displacement curve with the local tracking algorithm for the two cases of performing end-of-step updating and updating within iterations.
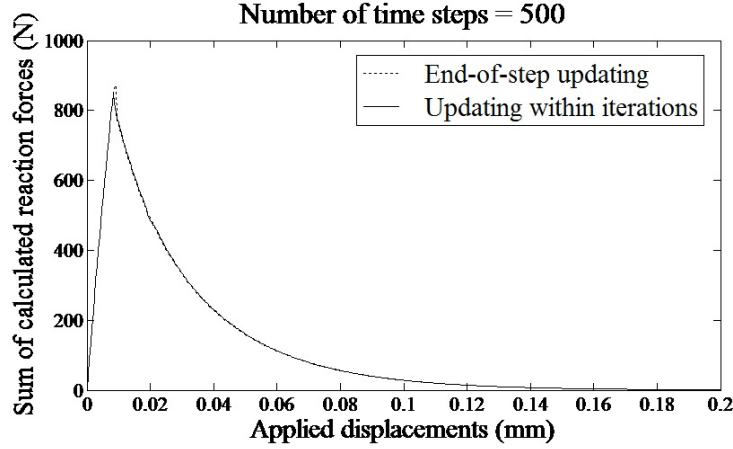

Figure 18: Double-edge notched specimen under tension (5-mm notch offset). Using 500 time steps, force-displacement curve with the local tracking algorithm for the two cases of performing end-of-step updating and updating within iterations.

beyond the root element since it reaches a previously traced band element. However, the localized deformation is captured across a continuous row of elements, as shown in Fig. 16b. For the case of updating within iterations, one dominant band forms that includes the two elements with the most critical status, Fig. 16d. The tracking algorithm traces the band from the first root element (the more critical one) on the left-hand side of the specimen and propagates until reaching the other root element on the other side. It should be noted that the set of localized elements forming the bands are not identical for the two cases and surface trajectories have small differences at the right half of their paths.

Table 2: Double-edge notched specimen under tension (5-mm notch offset). Simulation time for different tracking strategies and updating schedules using 100 time steps.

Simulation type	Tracking strategy	Updating schedule	Simulation time (sec.)
Double-edge notched specimen under tension (5-mm notch offset)	Local tracking	End of step	2682.35
		Within iterations	3477.61
	Global tracking	End of step	2628.47
		Within iterations	3375.54

Figures 17 and 18 present the force-displacement curves of the considered simulation for 100 and 500 time steps, respectively. The graph patterns for the global tracking algorithm are similar. Each figure compares the two cases of performing updating at the end of each time increment and within iterations in a given time increment. As the number of time steps adopted increases, the end-of-step updating case approaches the case of updating within iterations. Similar difference patterns in the peak reaction forces, robustness quality, and computational cost are observed as in the previous example. Table 2 provides simulation time of the considered simulation for each tracking strategy and updating schedule employed.

6.2.2. Notch offset value of 15 mm

A 198-element coarse unstructured mesh is developed with blunt notch tips modeled on the sides, Fig. 19. The root elements are detected automatically by the tracking algorithm based on the most critical status, i.e., the element possessing the largest maximum principal stress. The two localization bands initiate from the root elements and do not meet at the
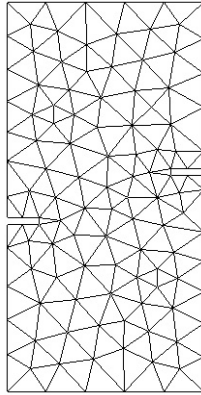

Figure 19: Double-edge notched specimen under tension (15-mm notch offset). Coarse unstructured meshing with automatic detection of the root elements.

specimen center mainly due to the different elevations of the root elements.

Two updating schedules for performing a tracking strategy are considered: end-of-step updating and updating within iterations. First, each updating schedule is carried out employing the local tracking algorithm, Box 1, and using 50 time steps as a starting point. The step size is then reduced by half to get more accurate results. The stabilizing crack tip technique was not required for this simulation. Table 3 provides the results. Figures 20 through 22 show the discontinuity surface paths for each case. The vertical displacement distributions are also provided for the case of using 200 time steps in Figs. 22c and 22f, where both updating schedules give acceptable results. Figures 23 through 25 compare the force-displacement curves for the two updating schedules.

The end-of-step updating fails to converge when large step sizes are used, as can be observed at Table 3. The reason for such performance is the rapid evolution of the two bands, which can be avoided by adopting a smaller step size. When using large step sizes, the set of localized elements intersected by the discontinuity surfaces at localization initiation are detected at the end of the step at which the onset of localization occurs. The delay in detecting the localization status, as a result of performing updating at the end of the step, imposes a stretching to the specimen without implementing the expected softening response. This inaccurate detection of localization introduces an extra number of localized elements to localization bands. These elements are then introduced to the global governing equations at the subsequent time step where difficulties in convergence are observed. Since the set of band elements are fixed at the end of the time step where localization was detected, the subsequent time step should handle the same set of band elements no matter how refined it

Table 3: Double-edge notched specimen under tension (15-mm notch offset). Numerical simulation results for using the local tracking algorithm.

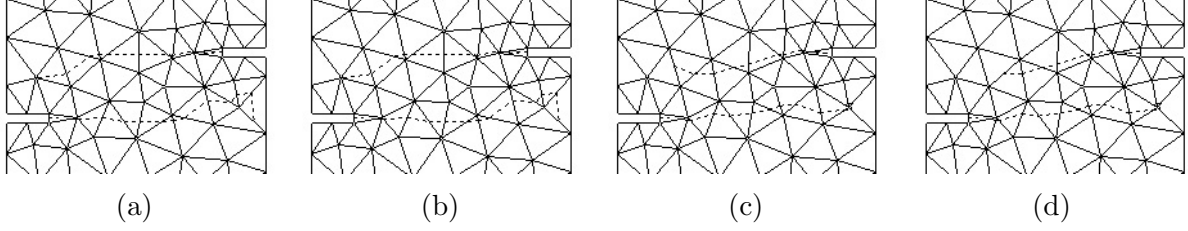| Simulation type	Updating schedule	Number of time steps	Results
Double-edge notched specimen under tension (15-mm notch offset)	End of step	50	Fails to converge
		100	Fails to converge
		200	Acceptable result
	Within iterations	50	Acceptable result
		100	Acceptable result
		200	Acceptable result

Figure 20: Double-edge notched specimen under tension (15-mm notch offset). Using 50 time steps, (a) the local tracking algorithm with end-of-step updating, dashed line represents the discontinuity surface paths (only for elements in the loading phase) at their maximum length, (b) at the last converged step, (c) the local tracking algorithm with updating within iterations, surface paths at their maximum length, (d) at the end of the simulation.
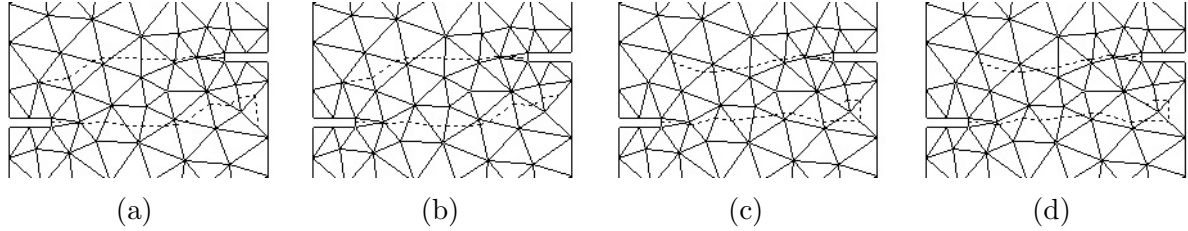

Figure 21: Double-edge notched specimen under tension (15-mm notch offset). Using 100 time steps, (a) the local tracking algorithm with end-of-step updating, dashed line represents the discontinuity surface paths (only for elements in the loading phase) at their maximum length, (b) at the last converged step, (c) the local tracking algorithm with updating within iterations, surface paths at their maximum length, (d) at the end of the simulation.

gets by performing step cut. Performing updating within iterations gives acceptable results even if large step sizes are used, as shown in Table 3. Detecting the band elements is performed within iterations at the time step in which the onset of localization occurs. This is a more accurate estimation in terms of detecting the band elements at a point closer to the exact time of localization initiation. Therefore, there is less artificial stressing imposed to the specimen, i.e., softening starts earlier compared to the end-of-step updating case.

The discontinuity surface paths for the end-of-step updating using 50 time steps are depicted in Figs. 20a and 20b at two points of the simulation; one when the surfaces are at their maximum length, and the other at the last converged step. The two bands are formed with each having extra localized elements at their tails (compared to the case of using a refined step size, see Fig. 22a). The length of the bands remains unchanged until the simulation failure. In addition, comparing with the case of updating within iterations, Fig. 20c, a longer top band and different trajectories are observed. Because of the longer band, the simulation faces difficulty in converging a few steps after localization initiation,
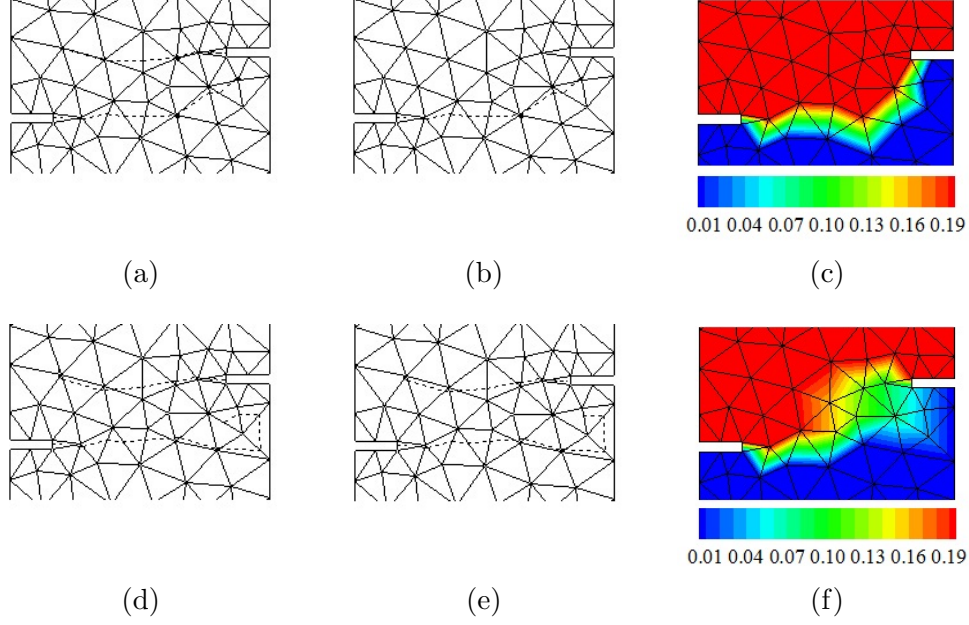
Figure 22: Double-edge notched specimen under tension (15-mm notch offset). Using 200 time steps, (a) the local tracking algorithm with end-of-step updating, dashed line represents the discontinuity surface paths (only for elements in the loading phase) at their maximum length, (b) at the end of the simulation, (c) deformed finite element mesh along with vertical displacement distribution at the end of the simulation, (d) the local tracking algorithm with updating within iterations, surface paths at their maximum length, (e) at the end of the simulation, (f) deformed finite element mesh along with vertical displacement distribution at the end of the simulation.

where a step cut is performed in order to get convergence. However, the simulation finally fails to converge. For updating within iterations, the simulation runs without facing any convergence issues and the two localization bands remain active (with an unloading at the tail for the top band) until the simulation ends, Fig. 20d. A similar elongated band pattern is observed for the case of using 100 time steps, Fig. 21a. Multiple step cuts can be observed few steps after localization initiation on the force-displacement graph in Fig. 24, where the simulation requires a high amount of computational effort in order to converge. The increased stressing due to the delayed localization detection plays a key role in forming elongated bands, which then results in making the simulation fail. Those failed simulations give acceptable results when the bands are limited in propagating beyond specified elements, i.e., the effect of artificial increased stress is eliminated by defining prescribed admissible regions for localization evolution.

The simulation was also performed using 200 time steps to compare the two updating schedules when a refined step size is adopted. In this case, the step size is small enough so
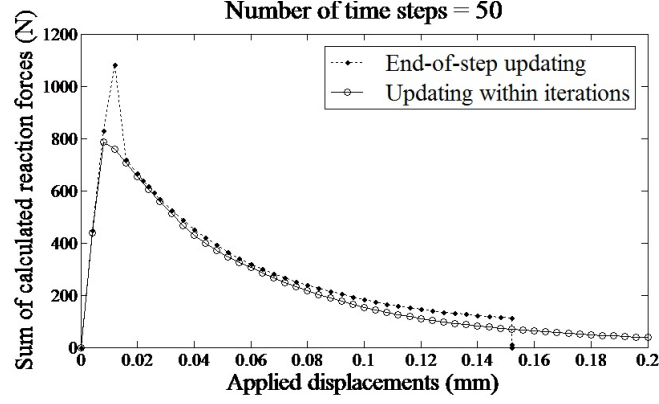
Figure 23: Double-edge notched specimen under tension (15-mm notch offset). Using 50 time steps, force-displacement curve with the local tracking algorithm for the two cases of performing end-of-step updating and updating within iterations.
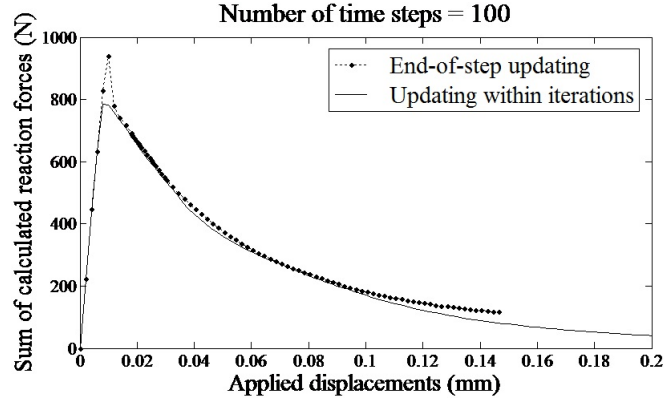

Figure 24: Double-edge notched specimen under tension (15-mm notch offset). Using 100 time steps, force-displacement curve with the local tracking algorithm for the two cases of performing end-of-step updating and updating within iterations.
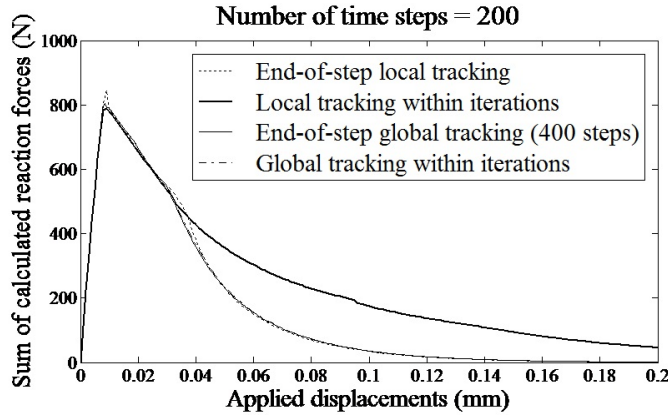

Figure 25: Double-edge notched specimen under tension (15-mm notch offset). Using 200 time steps, force-displacement curve with the local and global tracking algorithms for the two cases of performing end-of-step updating and updating within iterations. The global tracking algorithm with end-of-step updating graph corresponds to the 400-step case since 200-step case failed to capture an acceptable result.
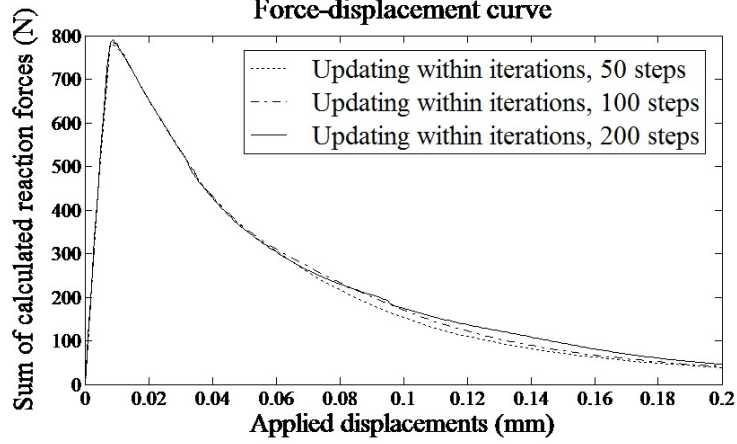
Figure 26: Double-edge notched specimen under tension (15-mm notch offset). Force-displacement curve with the local tracking algorithm for the case of performing updating within iterations using 50, 100, and 200 time steps.

both approaches are capable of providing acceptable results, though band trajectories still have minor differences. End-of-step updating ends up with one dominant band on the lower half of the specimen where the top band is entirely in the unloading regime, Figs. 22b and 22c. For updating within iterations, however, both bands remain in the loading phase where most of the vertical deformation tends to localize to the lower band, Figs. 22e and 22f. The left half of the strain localization zone shows how the vertical displacement distribution is concentrated along a continuous row of localized elements though two separate bands are capturing the failure response of the specimen. Figure 25 compares the force-displacement curves for the adopted updating schedules. End-of-step updating shows less energy dissipation, which corresponds to the one dominant band forming, compared to updating within iterations where two bands capture the softening response. The force-displacement curves for updating within iterations using 50, 100, and 200 time steps are presented in Fig. 26, where the graphs are fairly analogous.

With regard to accuracy, similar difference patterns in the peak reaction forces are observed as in the 5-mm notch offset case. In terms of robustness, it is observed that updating within iterations provides a more robust algorithm. Such updating schedule enables the use of arbitrary step sizes within a reasonable range. However, the end-of-step updating schedule may result in failure to converge when large step sizes are used and therefore produces some limitations on using large step sizes. As for comparing the computational cost,

39

Table 4: Double-edge notched specimen under tension (15-mm notch offset). Numerical simulation results for using the global tracking algorithm.

Simulation type	Updating schedule	Number of time steps	Results
Double-edge notched specimen under tension (15-mm notch offset)	End of step	50	Fails to converge
		100	Acceptable result
		200	Incorrect result
		400	Acceptable result
	Within iterations	50	Fails to converge
		100	Fails to converge
		200	Acceptable result
		400	Acceptable result

updating within iterations is still considered as a relatively more computationally expensive approach though end-of-step updating has shown some increased computational effort in getting convergence for few steps after localization initiation when large step sizes are used.

The simulation was also performed using the global tracking algorithm, Box 3. The results are presented in Table 4 for using 50, 100, 200, and 400 time steps. Both updating schedules fail when large step sizes are used. Acceptable results are obtained as step size is refined. All successful results emerging from the global tracking strategy contain one dominant band, either upper or lower one, which starts from one notch tip and reaches the other side of the specimen. The local tracking strategy reveals similar localization patterns though less concentrated localizations were sometimes observed, see Fig. 22f, and the discontinuity surfaces did not reach the specimen sides. For the case of using the global tracking strategy, the simulation was often observed to face numerical difficulties when switching from two bands in the loading phase to one dominant band. Refined step size implemented by step cuts helped to surmount the convergence difficulties. The force-displacement curves for the two adopted updating schedules are compared in Fig. 25. The two graphs are almost identical, and have minor differences (smaller reaction forces at the point of switching from two active bands into one dominant band) compared with the case that uses the local tracking algorithm with end-of-step updating. Therefore, except for the mentioned switching point, the force-displacement curves are almost identical when one dominant band forms regardless of both the updating schedule employed and whether the dominant band reaches the head-on specimen side or not.

The local and global tracking algorithms reveal almost identical band trajectories except for the tail parts. While the local tracking strategy tends to capture a returning pattern at the band tails, see Fig. 22e for example, the global tracking smooths out the localization orientation and often results in bands propagating through the whole width of the specimen. The results of the local tracking strategy better match with the experimental results reported in [Shi et al., 2005] where the two cracks are observed to curl around each other without tracing the whole specimen's width. It should be noted that the aforementioned report only provides a typical crack path pattern that was commonly observed throughout the experiments and the possibility for other trajectories, e.g., cracks reaching specimen sides, should also be considered. Such variety of possible crack paths becomes a more probable scenario when significant inhomogeneities exist within the material, such as in concrete, which is the material type modeled here. Eventually, these inhomogeneities should cause one band to open and the other to unload elastically. Here, however, we rely on numerical differences in the mesh and algorithm to trigger the loss of symmetry seen here. Such problems are known to be difficult to simulate numerically. To determine the likely true responses, a statistical analysis with accurate variations in the material properties is necessary. Such an analysis is beyond the scope of this work, and the accuracy of the tails of the curves can be questioned (though probably both are within the range of physical responses). What can be concluded is that global tracking tends to smooth out the fracture path.

6.3. Stretching of a block with local imperfection

The last example consists of a plane strain stretching of a block with local imperfection, as shown in Fig. 27a. The imperfection can be in the form of a damaged area, pre-developed micro cracks/voids, etc., which is implicitly modeled by a finite element with reduced tensile strength located at the left-hand side of the specimen. In previous examples, the entire localization surfaces formed almost instantly within one or a few time steps due to the homogeneous or nearly homogeneous nature of the problems. This example is set up to have a relatively gradual evolution of the discontinuity surface in order to provide the capability of performing the designated comparative studies for the two updating schedules. The material is linear elastic and isotropic with Young's modulus $E = 5.5E+03$ MPa and Poisson's ratio

$\nu = 0.25$. The parameters used to describe the exponential softening function, Eq. 11, are tensile strength $f_t = 4.0E+01$ MPa and fracture energy $G_F = 5.0E+01$ N/mm. A displacement-controlled approach is carried out by applying triangular upward prescribed displacement on the top side of the specimen. Maximum deformation, $d = 0.01$ m, is imposed on the left-hand side. A 230-element coarse unstructured mesh has been developed using a standard constant strain triangle (CST) finite element, Fig. 27b. One element ,the highlighted element in the figure, with degraded tensile strength and fracture energy of one tenth of the original values (i.e., $f_t = 4.0E+00$ MPa and $G_F = 5.0E+00$ N/mm) is embedded on the left-hand side of the specimen to implicitly model the local imperfection.

The local tracking algorithm, Box 1, equipped with the stabilizing crack tip technique, Box 2, was used for tracking purpose. The global tracking strategy was also used, but the force-displacement curves were very similar. Hence, we focus our discussion of this part on the local tracking results. The discontinuity surface paths for different updating schedules and the deformed finite element mesh with vertical displacement distribution are illustrated in Fig. 28. At localization initiation, the discontinuity surface starts to evolve from the location of the imperfection. As the simulation continues, the surface evolves following an
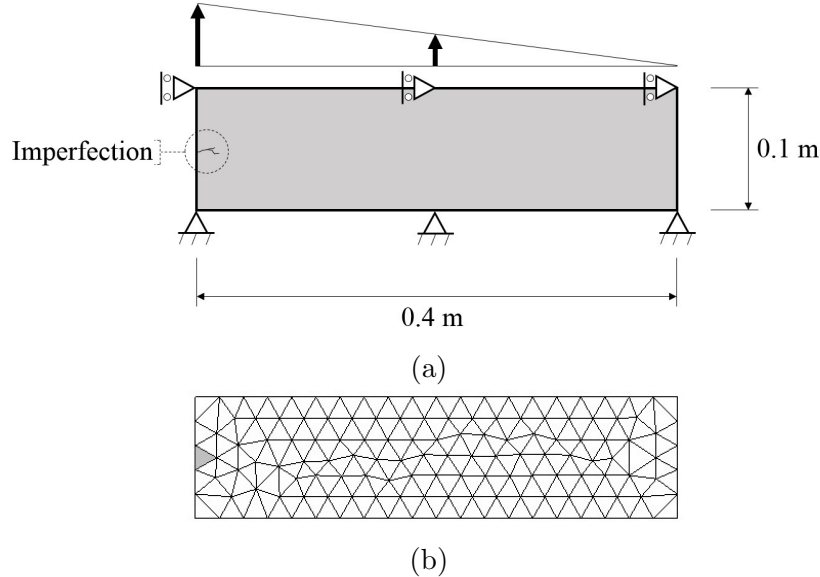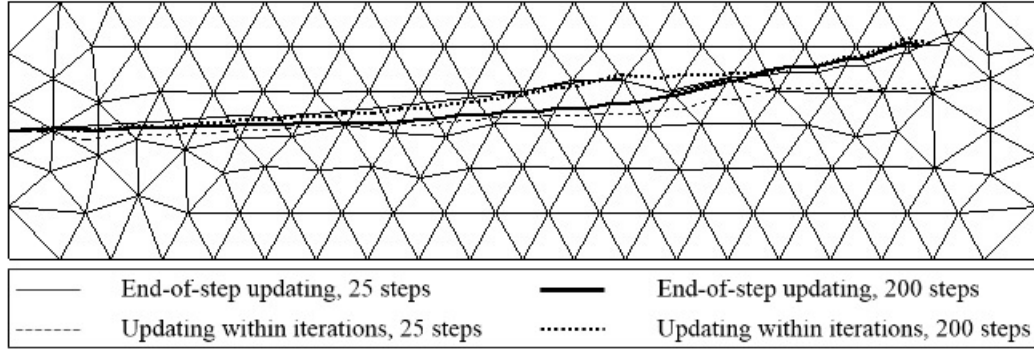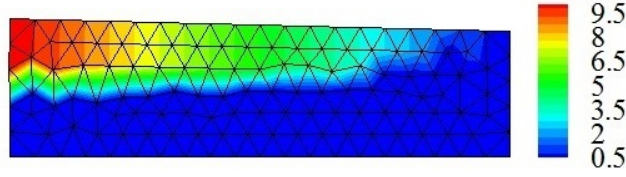

(a)

(b)

Figure 27: Stretching of a block with local imperfection. (a) Dimensions, loading, and boundary conditions, (b) coarse unstructured finite element meshing. The element representing the local imperfection is highlighted on the left-hand side.

(a)

(b)

Figure 28: Stretching of a block with local imperfection. Using the local tracking algorithm, (a) the discontinuity surface paths (only for elements in the loading phase) for performing end-of-step updating using 25 steps (fine solid line), updating within iterations (fine dashed line), end-of-step updating using 200 steps (bold solid line), updating within iterations (bold dotted line), (b) deformed finite element mesh along with vertical displacement distribution for performing end-of-step updating using 200 steps.

inclined path towards the right-hand upper corner of the specimen. The softening response is captured throughout a set of localized elements forming an inclined strain localization band. As shown in Fig. 28a, the employed updating schedules, end-of-step updating and updating within iterations, using 200 time steps (bold solid and dotted lines) give an approximately identical discontinuity surface paths, except for the middle part where end-of-step updating gives a lower surface trajectory. The surface paths for the case of using 25 time steps (fine solid and dashed lines) show some other differences. End-of-step updating gives a longer and more inclined path, while updating within iterations reveals a relatively closer trajectory to the more accurate results of the simulations using 200 time steps.

Figure 29 provides the force-displacement curves for the simulations equipped with the local tracking algorithm using 25 and 200 time steps. The horizontal axis represents the vertical displacement imposed only on the node located at the far left side of the specimen, which experiences the maximum applied deformation. The vertical axis indicates the total calculated reaction forces in vertical orientation for all the nodes located on the top edge.
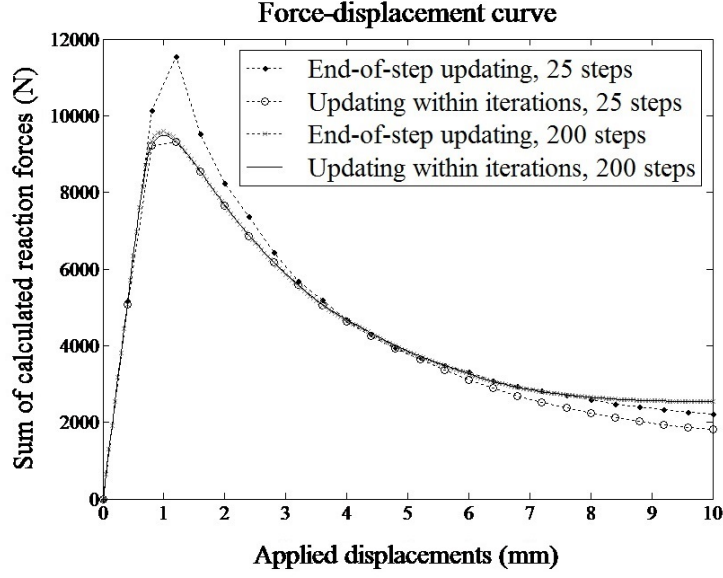
43

Figure 29: Stretching of a block with local imperfection. Force-displacement curves for using the local tracking algorithm considering the two cases of end-of-step updating and updating within iterations using 25 and 200 time steps.
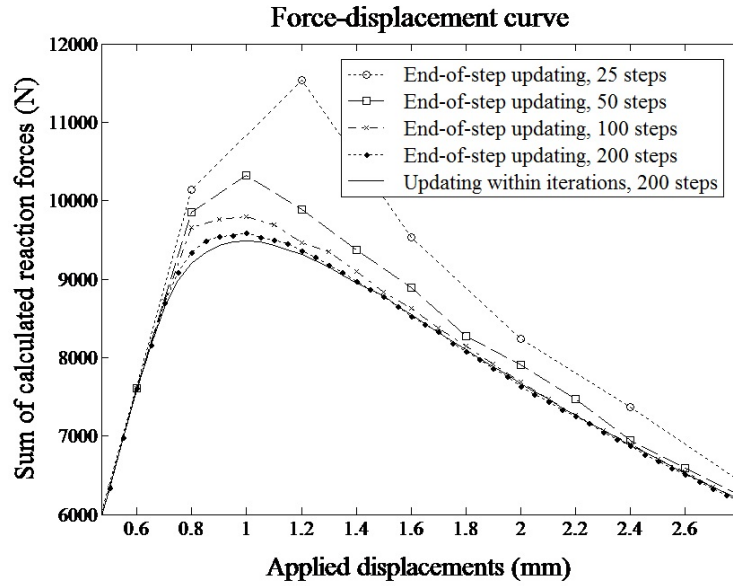

Figure 30: Stretching of a block with local imperfection. Force-displacement curves zoomed in around peak force, the end-of-step updating case approaches updating within iterations as time step size is refined.

The figure compares the two cases of performing end-of-step updating and updating within iterations. For using 25 steps, end-of-step updating has a higher peak stress and slightly higher residual stress as the localization surface evolves, which is an incorrect estimation. As seen in the earlier examples, the generated inaccuracy originates from the delayed detection

44

of the localization status, and keeps building up as the localization surface evolves. Except for this localization evolution part of the simulation, i.e., for the preliminary elastic response and when no localization propagation is observed, the two force-displacement curves agree very closely. The difference in the reaction forces starts to alleviate as the time step size is refined, i.e., the end-of-step updating case approaches updating within iterations. The graph patterns for using the global tracking algorithm are similar.

Figure 30 shows the force-displacement curves for a simulation using the local tracking algorithm, which is magnified around the peak value of the reaction forces. The end-of-step updating case is performed using 25, 50, 100, and 200 time steps. A softer response is captured as the step size is refined and the force-displacement curve approaches the case of updating within iterations using 200 steps. Interestingly, updating within iterations generates a smoother force-displacement curve even compared to the end-of-step updating case with 200 steps.

Figure 29 also compares the force-displacement curves for the simulations with the local tracking algorithm performed within iterations using 25 and 200 time steps. In contrast to the case of end-of-step updating, Fig. 30, where a considerable amount of difference in the estimated reaction forces was observed, less difference is generated for updating within iterations. As is shown in Fig. 29, the force-displacement curve for the case of using 25 time steps almost follows the curve of 200 time steps (notice the marker locations on the curve), except for approximately the second half of the simulation where a softer response is captured due to the different surface paths each case reveals.

In terms of accuracy of the two updating schedules, they reveal similar localization trajectories, though some differences in surface length and inclination are observed. For end-of-step updating, artificially increased reaction forces, leading to inaccurate higher estimations of energy dissipation, are also generated for a longer range around the peak value in the force-displacement curves. This longer range is built because of the relatively gradual propagation of the localization surface. For an ongoing localization evolution, the end-of-step updating results in a delayed detection of newly localized elements, which then imposes artificial loading to the specimen. Similar difference patterns in robustness and computational cost are observed as in the first example (stretching of a homogeneous block). Due to the gradual

Table 5: Stretching of a block with local imperfection. Simulation time for different tracking strategies and updating schedules using 25 time steps.

Simulation type	Tracking strategy	Updating schedule	Simulation time (sec.)
Stretching of a block with local imperfection	Local tracking	End of step	1081.58
		Within iterations	1829.74
	Global tracking	End of step	975.59
		Within iterations	1678.37

formation of the discontinuity surface, the artificial increased stress of the specimen, imposed when using the end-of-step updating, does not create convergence issues, unlike the nearly homogeneous examples. Table 5 provides the simulation time for each tracking strategy and updating schedule employed.

Table 6 shows the utilization of the stabilizing crack tip technique, Box 2, implemented within the local tracking algorithm. The method is needed for the end-of-step updating case using large step sizes (25 and 50 time steps). However, as the step size is refined, this technique is not needed. Smoother discontinuity paths, perhaps as a result of lower stress gradients, eventually eliminate the need for the stabilizing technique. Performing updating within iterations does not require the technique even for large step sizes since it captures a more accurate softening response. This is in accordance with the notion that the end-of-step updating with large step sizes raises inaccuracy issues. The global tracking strategy is also capable of tracking a smoother discontinuity surface trajectory without the need for the stabilizing technique.

Table 6: Stretching of a block with local imperfection. Utilization of the stabilizing crack tip technique.

Tracking strategy	Updating schedule	Number of time steps	Number of times stabilizing used	Change in orientation (exceeding $\theta_{\mathrm{allowed}}$)
Local tracking	End of step	25	2	155.67°, 168.25°
		50	1	171.64°
		100, 200	0	n/a
	Within iterations	25, 50, 100, 200	0	n/a
Global tracking	(either case)	25, 50, 100, 200	n/a	n/a

7. Concluding remarks

In this study, some numerical aspects of different band updating schedules in modeling strain localization problems are investigated. One schedule is based on updating fracture path information at the end of each time step, the other by updating within iterations in a given time step. A comparison between local and global tracking algorithms has also been made. Investigating each of these approaches and performing a comparative study have been done by modeling some numerical examples.

To investigate the performance of the schedules, the localization is set up to initiate when the maximum principle stress exceeds a given tensile strength. The direction orthogonal to the maximum principal stress direction has been taken as the orientation of the localized surface. A traction-separation relationship in the spirit of damage mechanics has been employed to determine displacement jumps along localization surfaces. Embedded in enhanced finite element framework, local and global tracking strategies have been tested for tracking localization surface paths. The following observations have been made:

- *Robustness*: Updating within iterations has been generally observed to provide a more robust numerical algorithm, while end-of-step updating has sometimes failed to reach an expected result. The reason for such performance is the more accurate estimation of softening response developed by the former approach. For modeling nearly homogeneous problems using large step sizes, the end-of-step updating loses the capability to accurately capture peak stresses, discontinuity surface lengths and dissipated energy. This effect has been observed leading to global failure of the simulation where even performing multiple step cuts could not find a converged solution. However, reducing step size did improve robustness. Updating within iterations has been also observed to experience a slower rate of convergence. Such sub-quadratic convergence in global Newton-Raphson iterations might cause robustness issues in some complex problems, though it did not raise any issues for the simulations in this study.

- *Accuracy*: Large step sizes with updating at the end of each time step can introduce inaccuracies in length of localized bands as well as the force-displacement curves. The latter difference is marked by over-prediction of reaction forces, notably peak force,

which corresponds to incorrect estimation of the amount of energy dissipated by the localized region. The reason for this overestimation is the delayed detection of the set of localized elements intersected by the discontinuity surfaces (band elements) at the end of the step at which the onset of localization occurs. Such a lag in a given localization detection process imposes an artificial extra loading to the specimen before implementing the designated softening. The inaccurate estimation of localization status may introduce extra number of localized elements to the localization bands which then may cause convergence issues in the solution of global governing equations. However, updating within iterations allows improvement of the length and orientation of localization bands during the iteration procedure. Therefore, the length of the localized region can be modified (typically corrected) before localization orientation is fixed by the end of the time step.

In homogeneous and nearly homogeneous problems where the entire localization surfaces form almost instantly within one or a few time steps, end-of-step updating using large step sizes can over-predict peak force compared to the case of updating within iterations. Hence, the extra propagation of localization surfaces occurs around this time. For problems involving a relatively gradual band formation, such inaccurate estimation of energy dissipation continues through the propagation given an ongoing localization evolution. The two updating schedules tend to agree as the step size is refined. For smaller time steps, end-of-step updating becomes capable of determining the localization status more accurately, and fewer inaccuracies are observed. The performance typically improves as more time steps are used. In terms of inter-element spatial location and orientation of discontinuity surfaces, the two approaches have been generally found to be similar, especially on time step refinement.

- *Computational cost*: More time and computational effort have been observed when updating is carried out for each single iteration at least in cases where a large number of step cuts are not necessary for end-of-step updating. Two major factors for such increased computational cost have been identified. One is the extra number of times that the tracking subroutine is called since updating is performed for each iteration,

compared to the end-of-step updating case where the subroutine is called only once for a given time step. The other factor corresponds to the slower rate of convergence for a given evolving localization that results in additional iterations before reaching a converged solution. Embedding the set of softening elements within the global-level governing equations during the iterative solution is considered to be the reason for such a relatively slower convergence. Quadratic convergence is recovered when no further localization propagation occurs. On the other hand, the end-of-step updating has been observed to follow a quadratic convergence rate, and sometimes faster depending on the problem being solved.

Overall, updating within iterations captures a relatively more accurate softening response at the expense of higher computational cost compared to the end-of-step updating. It is then down to one's preferences to select one of the approaches while trying to balance the computational cost and accuracy needs for a strain localization problem at hand. It should also be noted that the end-of-step updating schedule using large step sizes can result in less robust algorithms, and is not recommended for modeling nearly homogeneous problems where rapid propagation of discontinuity surfaces are observed.

The enhanced finite element framework was employed in this study to model strong discontinuities in the form of fractures, and the conclusions derived above refer primarily to those type of discontinuities. However, there is this implicit understanding that some observations and conclusions apply in numerical modeling of weak discontinuities as well.

Appendix A. Residual term for balance on a discontinuity surface and numerical implementation

Appendix A.1. Residual term and derivatives

The residual expression for balance on a discontinuity surface in matrix form, Eq. 17, is given as

$$\boldsymbol{r}_e = \left(\frac{f\left(\tilde{w}_e\right)}{\tilde{w}_e} \mathbf{1} + [\boldsymbol{n}_e] \cdot [\boldsymbol{C}^e] \cdot \left[\boldsymbol{\nabla} f_e^h\right] \right) \cdot \boldsymbol{w}_e - [\boldsymbol{n}_e] \cdot [\boldsymbol{C}^e] \cdot \left\{ \boldsymbol{\varepsilon}_e^{h\,\mathrm{conf}} \right\} = \mathbf{0} \qquad (A.1)$$

where $\mathbf{1}$ is a 2-by-2 identity matrix. The reader is referred to Section 4 for definition of other parameters. The expanded description, showing the array form of the matrices and vectors of Eq. A.1, can be represented in Voigt notation as

$$
\left\{ \begin{array}{c} \frac{f(\tilde{w}_e)}{\tilde{w}_e} w_{ex} \\ \frac{f(\tilde{w}_e)}{\tilde{w}_e} w_{ey} \end{array} \right\} +
$$

$$
\begin{bmatrix} n_{ex} & 0 & n_{ey} \\ 0 & n_{ey} & n_{ex} \end{bmatrix} \cdot \begin{bmatrix} c(1-\nu) & c\nu & 0 \\ c\nu & c(1-\nu) & 0 \\ 0 & 0 & G \end{bmatrix} \cdot \left\{ \begin{array}{c} w_{ex} f^h_{e\,,x} \\ w_{ey} f^h_{e\,,y} \\ w_{ex} f^h_{e\,,y} + w_{ey} f^h_{e\,,x} \end{array} \right\} -
$$

$$
\begin{bmatrix} n_{ex} & 0 & n_{ey} \\ 0 & n_{ey} & n_{ex} \end{bmatrix} \cdot \begin{bmatrix} c(1-\nu) & c\nu & 0 \\ c\nu & c(1-\nu) & 0 \\ 0 & 0 & G \end{bmatrix} \cdot \left\{ \begin{array}{c} \varepsilon^{h}_{e,\,xx}{}^{\text{conf}} \\ \varepsilon^{h}_{e,\,yy}{}^{\text{conf}} \\ \varepsilon^{h}_{e,\,xy}{}^{\text{conf}} \end{array} \right\} = \mathbf{0} \tag{A.2}
$$

where w_{ex} and w_{ey} are components of the displacement jump vector $\boldsymbol{w}_e$ in the global coordinates. The quantities n_{ex} and n_{ey} are components of the unit normal vector, $\boldsymbol{n}_e$, which is perpendicular to the discontinuity surface S pointing towards Ω_+ for each localized element e, as shown in Fig. 1b. The elastic modulus, $\boldsymbol{C}^e$, is expanded for the plane strain case, where ν represents the Poisson's ratio, G, the shear modulus, and c is defined as

$$
c = \frac{E}{(1+\nu)(1-2\nu)} \tag{A.3}
$$

and E is the Young's modulus. For a plane stress problem, the corresponding form of the elastic modulus is used. The terms $f^h_{e\,,x}$ and $f^h_{e\,,y}$ are summation of the gradient of the shape functions for the active nodes of a localized element e in x and y directions, respectively. The strain terms are shown as ε_{xx}, ε_{yy}, and ε_{xy}.

For a loading phase, the solid curve in Fig. 5b, Eq. A.2 represents a *nonlinear* balance equation. The nonlinearity arises from the dependence of $\tilde{w}_e$ on $\boldsymbol{w}_e$ as the discontinuity surfaces separate. By simplifying, the equation takes the form of

$$
\left\{ \begin{array}{c} f_1 \\ f_2 \end{array} \right\} = \mathbf{0}. \tag{A.4}
$$

Each of the quantities f_1 and f_2 represents one of the two balance equations emerging from the

resultant 2-by-1 matrix equation, Eq. A.2. This equation can be solved for the displacement jump vector components, w_{ex} and w_{ey}, using an element-level Newton-Raphson iterative solution algorithm, in which the iterative incremental values are explicitly calculated by

$$
\left\{ \begin{array}{c} \Delta w_{ex} \\ \Delta w_{ey} \end{array} \right\} = \left[\begin{array}{cc} \frac{\partial f_1}{\partial w_{ex}} & \frac{\partial f_1}{\partial w_{ey}} \\ \frac{\partial f_2}{\partial w_{ex}} & \frac{\partial f_2}{\partial w_{ey}} \end{array} \right]^{-1} \cdot \left\{ \begin{array}{c} -f_1 \\ -f_2 \end{array} \right\}.
\tag{A.5}
$$

The corresponding derivatives with respect to the displacement jump components in the global coordinates are

$$
\frac{\partial f_1}{\partial w_{ex}} = -c(1-\nu)f^h_{e,x}n_{ex} - Gf^h_{e,y}n_{ey} - \frac{w_{ex}^2}{\tilde{w}_e^3}f\left(\tilde{w}_e\right)\left[\tilde{w}_e\left(-\frac{f_t}{G_F}\right) - 1\right] - \frac{f\left(\tilde{w}_e\right)}{\tilde{w}_e}
\tag{A.6}
$$

$$
\frac{\partial f_1}{\partial w_{ey}} = -c\nu f^h_{e,y}n_{ex} - Gf^h_{e,x}n_{ey} - \frac{w_{ex}w_{ey}}{\tilde{w}_e^3}f\left(\tilde{w}_e\right)\left[\tilde{w}_e\left(-\frac{f_t}{G_F}\right) - 1\right]
\tag{A.7}
$$

$$
\frac{\partial f_2}{\partial w_{ex}} = -c\nu f^h_{e,x}n_{ey} - Gf^h_{e,y}n_{ex} - \frac{w_{ex}w_{ey}}{\tilde{w}_e^3}f\left(\tilde{w}_e\right)\left[\tilde{w}_e\left(-\frac{f_t}{G_F}\right) - 1\right]
\tag{A.8}
$$

$$
\frac{\partial f_2}{\partial w_{ey}} = -c(1-\nu)f^h_{e,y}n_{ey} - Gf^h_{e,x}n_{ex} - \frac{w_{ey}^2}{\tilde{w}_e^3}f\left(\tilde{w}_e\right)\left[\tilde{w}_e\left(-\frac{f_t}{G_F}\right) - 1\right] - \frac{f\left(\tilde{w}_e\right)}{\tilde{w}_e}.
\tag{A.9}
$$

It should be noted that $\tilde{w}_e$, which represents the historical maximum of the magnitude of the displacement jump vector for a localized element e, should be updated within Newton-Raphson iterations; i.e., each time a new jump increment is calculated by solving Eq. A.5, the corresponding effect on $\tilde{w}_e$ should be taken into account. For numerical implementation, $\tilde{w}_e$ is also recorded at the end of each time step, i.e., when a converged solution is reached, as $\tilde{w}_e^{\text{conv}}$. This end-of-step recording occurs regardless of the type of the adopted tracking strategy and updating schedule. By performing the iterative solution, the accumulated element-level displacement jump vector $\boldsymbol{w}_e$ is calculated. A relative convergence tolerance of $\text{tol}_{local} = 1.0\text{E}-08$ is assumed for the Newton-Raphson algorithm.

For the unloading/reloading regime, the dashed line in Fig. 5b, Eq. A.2 becomes a *linear* balance equation, since $\tilde{w}_e$ is a constant without any dependence on the displacement jump vector components. Therefore, the equation can be explicitly solved for the unknown jump terms using

$$
\boldsymbol{w}_e = \frac{[\boldsymbol{n}_e] \cdot [\boldsymbol{C}^e] \cdot \left\{\boldsymbol{\varepsilon}_e^{h\,\text{conf}}\right\}}{\frac{f(\tilde{w}_e)}{\tilde{w}_e}\mathbf{1} + [\boldsymbol{n}_e] \cdot [\boldsymbol{C}^e] \cdot [\boldsymbol{\nabla} f_e^h]}.
\tag{A.10}
$$

Box 4 represents an algorithmic summary of the calculation procedure of the displacement jump vector for a localized element performed at each global iteration.

Box 4: Summary of the calculation procedure of the displacement jump vector for a localized element.

Step 1: If a separation has already started in a previous time step ($\tilde{w}_e^{\text{conv}} \neq 0.$), assume unloading/reloading regime and solve explicitly for the jump unknowns using Eq. A.10 and update $\tilde{w}_e$. Otherwise, go to *Step 3*.

Step 2: If $\tilde{w}_e$ is less than $\tilde{w}_e^{\text{conv}}$, the assumption of unloading/reloading is correct and exit. Otherwise, go to *Step 3*.

Step 3: If $\tilde{w}_e = 0$, then assign $\tilde{w}_e = 1.0\text{E}-10$ to avoid zero denominators.

Step 4: Solve for the jump unknowns using the Newton-Raphson iterative solution algorithm, see Eqs. A.4 through A.9, and update $\tilde{w}_e$.

Remark 4. *Taking an initial guess is a requirement for the Newton-Raphson solution procedure. To solve for the element-level displacement jump vector here, such initial guess is in the form of a relatively small (compared to the specimen dimensions) displacement vector in global coordinates. The Newton-Raphson algorithm was often observed to face convergence issues when random initial guesses were taken. To entirely remove such numerical difficulties, it is suggested to take those initial values equal to a very small portion (of order 1.0E−10) of the traction vector on the discontinuity surface. This strategy has the physical logic of having the separation vector and its corresponding driving force in the same direction, and also is in accordance with one of the essential assumptions of the adopted cohesive crack model pointed out in Section 3, i.e., the traction vector is parallel to the displacement jump vector across the discontinuity interfaces, as is shown in Eq. 9.*

Appendix A.2. Numerical implementation

In this subsection, two flowcharts are provided in order to illustrate the numerical algorithm employed to model strain localization problems. Figure A.31 gives a schematic representation of the overall solution algorithm. The loop included in the flowchart corresponds to the time discretization of the simulation. At each time step, the Newton-Raphson subroutine is called to solve for global governing equations of the boundary value problem. The relative tolerance for global convergence is taken as $\text{tol}_{global} = 1.0\text{E}-08$.

Figure A.32 illustrates a flowchart for the Newton-Raphson iterative algorithm, which is embedded as a subroutine in the first flowchart, Fig. A.31. A subroutine to calculate the residual vector performs the element-level calculations including element internal and

external forces, stiffness, and residual, along with the global-level assemblages. The localized elements are also treated accordingly. If the end-of-step updating schedule is considered, the localized elements will be determined based on the localization status at the end of a previous step for a given time increment. Nevertheless, for the case of updating within iterations, the corresponding data will be based upon the localization status at the end of a previous iteration for a given iteration. For the first iteration, such data will emerge from the end of a previous step.

For both updating schedules, end-of-step and within iterations, localization orientation should get fixed by the end of each time increment, i.e., when a converged solution is reached. This is in accordance with reality observation that whenever a displacement discontinuity is formed, the discontinuity surface orientation remains constant. Within the local tracking algorithm, this task is done by fixing the unit vector normal to the discontinuity surface,
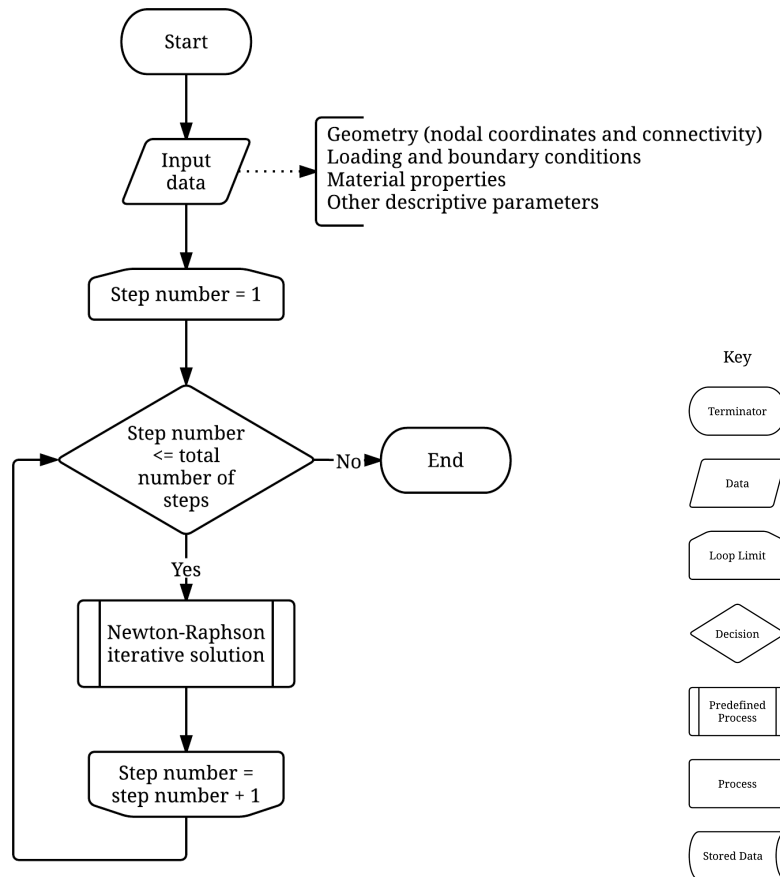
Figure A.31: Representation of the overall solution algorithm.

and by keeping the nodal temperature of band element nodes constant if the global tracking strategy is adopted. Displacement, strain, and stress fields along with reaction forces are stored at the end of each time step for plotting the results.
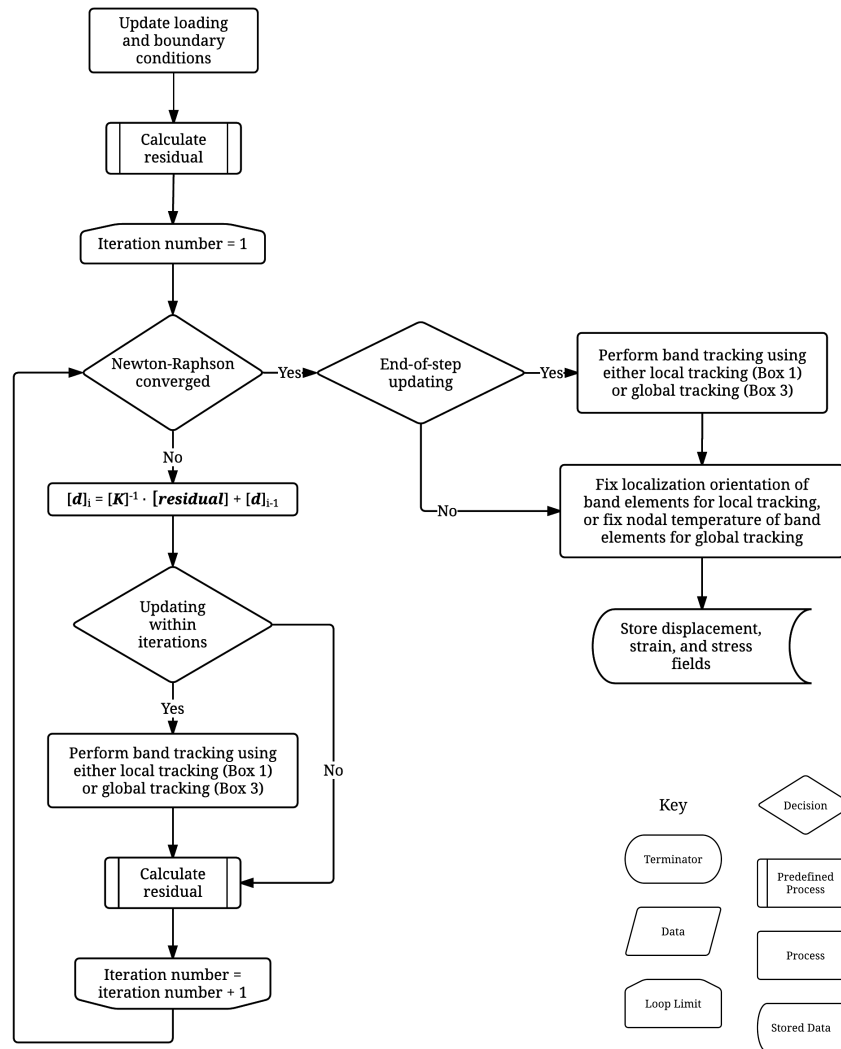
Acknowledgements

Figure A.32: Newton-Raphson iterative algorithm.

References

Alfaiate, J., Wells, G., Sluys, L., 2002. On the use of embedded discontinuity elements with crack path continuity for mode-i and mixed-mode fracture. Engineering Fracture Mechanics 69 (6), 661–686.

Anderson, T. L., 2005. Fracture mechanics: fundamentals and applications. CRC press.

Armero, F., Garikipati, K., 1996. An analysis of strong discontinuities in multiplicative finite strain plasticity and their relation with the numerical simulation of strain localization in solids. International Journal of Solids and Structures 33 (20), 2863–2885.

Barenblatt, G. I., 1962. The mathematical theory of equilibrium cracks in brittle fracture. Advances in applied mechanics 7 (1), 55–129.

Batra, R., Zhang, G., 2004. Analysis of adiabatic shear bands in elasto-thermo-viscoplastic materials by modified smoothed-particle hydrodynamics (msph) method. Journal of computational physics 201 (1), 172–190.

Belytschko, T., Gu, L., Lu, Y., 1994. Fracture and crack growth by element free galerkin methods. Modelling and Simulation in Materials Science and Engineering 2 (3A), 519.

Belytschko, T., Krongauz, Y., Organ, D., Fleming, M., Krysl, P., 1996. Meshless methods: an overview and recent developments. Computer methods in applied mechanics and engineering 139 (1), 3–47.

Belytschko, T., Moës, N., Usui, S., Parimi, C., 2001. Arbitrary discontinuities in finite elements. International Journal for Numerical Methods in Engineering 50 (4), 993–1013.

Biabanaki, S., Khoei, A., 2012. A polygonal finite element method for modeling arbitrary interfaces in large deformation problems. Computational Mechanics 50 (1), 19–33.

Borja, R. I., 2000. A finite element model for strain localization analysis of strongly discontinuous fields based on standard galerkin approximation. Computer Methods in Applied Mechanics and Engineering 190 (11), 1529–1549.

Borja, R. I., Regueiro, R. A., 2001. Strain localization in frictional materials exhibiting displacement jumps. Computer Methods in Applied Mechanics and Engineering 190 (20), 2555–2580.

Boyce, B. L., Kramer, S. L., Fang, H. E., Cordova, T. E., Neilsen, M. K., Dion, K., Kaczmarowski, A. K., Karasz, E., Xue, L., Gross, A. J., et al., 2014. The sandia fracture challenge: blind round robin predictions of ductile tearing. International Journal of Fracture 186 (1-2), 5–68.

Camacho, G. T., Ortiz, M., 1996. Computational modelling of impact damage in brittle materials. International Journal of solids and structures 33 (20), 2899–2938.

Carol, I., Prat, P. C., López, C. M., 1997. Normal/shear cracking model: application to discrete crack analysis. Journal of engineering mechanics 123 (8), 765–773.

Cendón, D., Gálvez, J., Elices, M., Planas, J., 2000. Modelling the fracture of concrete under mixed loading. International Journal of Fracture 103 (3), 293–310.

Chen, J.-S., Chi, S.-W., Hu, H.-Y., 2011. Recent developments in stabilized galerkin and collocation meshfree methods. Computer Assisted Mechanics and Engineering Sciences 18, 3–21.

Cosserat, E., Cosserat, F., 1909. Théorie des corps déformables. Herman et Fils, Paris.

De Borst, R., 2003. Numerical aspects of cohesive-zone models. Engineering fracture mechanics 70 (14), 1743–1757.

De Borst, R., Sluys, L., 1991. Localisation in a cosserat continuum under static and dynamic loading conditions. Computer Methods in Applied Mechanics and Engineering 90 (1), 805–827.

Duarte, C. A., Babuška, I., Oden, J. T., 2000. Generalized finite element methods for three-dimensional structural mechanics problems. Computers & Structures 77 (2), 215–232.

Duarte, C. A., Hamzeh, O., Liszka, T., Tworzydlo, W., 2001. A generalized finite element method for the simulation of three-dimensional dynamic crack propagation. Computer Methods in Applied Mechanics and Engineering 190 (15), 2227–2262.

Dugdale, D., 1960. Yielding of steel sheets containing slits. Journal of the Mechanics and Physics of Solids 8 (2), 100–104.

Elices, M., Guinea, G., Gomez, J., Planas, J., 2002. The cohesive zone model: advantages, limitations and challenges. Engineering fracture mechanics 69 (2), 137–163.

Fleming, M., Chu, Y., Moran, B., Belytschko, T., Lu, Y., Gu, L., 1997. Enriched element-free galerkin methods for crack tip fields. International journal for numerical methods in engineering 40 (8), 1483–1504.

Foster, C. D., 2006. Modeling variable friction and slip weakening of localized geomaterials using an embedded strong discontinuity finite element. Ph.D. thesis, Stanford University.

Foster, C. D., Borja, R., Regueiro, R., 2007. Embedded strong discontinuity finite elements for fractured geomaterials with variable friction. International Journal for Numerical Methods in Engineering 72 (5), 549–581.

Fries, T.-P., Belytschko, T., 2010. The extended/generalized finite element method: an overview of the method and its applications. International Journal for Numerical Methods in Engineering 84 (3), 253–304.

Gálvez, J., Cendón, D., Planas, J., 2002. Influence of shear parameters on mixed-mode fracture of concrete. International Journal of Fracture 118 (2), 163–189.

Hashemian, A., Shodja, H., 2008. Gradient reproducing kernel particle method. Journal of Mechanics of Materials and Structures 3 (1), 127–152.

Hillerborg, A., 1991. Application of the fictitious crack model to different types of materials. International Journal of Fracture 51 (2), 95–102.

Hillerborg, A., Modéer, M., Petersson, P.-E., 1976. Analysis of crack formation and crack growth in concrete by means of fracture mechanics and finite elements. Cement and concrete research 6 (6), 773–781.

Jirásek, M., 2000. Comparative study on finite elements with embedded discontinuities. Computer Methods in Applied Mechanics and Engineering 188 (1), 307–330.

Jirásek, M., Rolshoven, S., 2003. Comparison of integral-type nonlocal plasticity models for strain-softening materials. International Journal of Engineering Science 41 (13), 1553–1602.

Khoei, A., Biabanaki, S., Anahid, M., 2008. Extended finite element method for three-dimensional large plasticity deformations on arbitrary interfaces. Computer Methods in Applied Mechanics and Engineering 197 (9), 1100–1114.

Khoei, A., Yadegari, S., Biabanaki, S., 2010. 3d finite element modeling of shear band localization via the micro-polar cosserat continuum theory. Computational Materials Science 49 (4), 720–733.

Khoei, A. R., 2014. Extended Finite Element Method: Theory and Applications. John Wiley & Sons.

Klein, P., Foulk, J., Chen, E., Wimmer, S., Gao, H., 2001. Physics-based modeling of brittle fracture: cohesive formulations and the application of meshfree methods. Theoretical and Applied Fracture Mechanics 37 (1), 99–166.

Liu, W. K., Chen, Y., Jun, S., Chen, J., Belytschko, T., Pan, C., Uras, R., Chang, C., 1996. Overview and applications of the reproducing kernel particle methods. Archives of Computational Methods in Engineering 3 (1), 3–80.

Liu, W. K., Hao, S., Belytschko, T., Li, S., Chang, C. T., 1999. Multiple scale meshfree methods for damage fracture and localization. Computational materials science 16 (1), 197–205.

Liu, W. K., Jun, S., Zhang, Y. F., 1995. Reproducing kernel particle methods. International journal for numerical methods in fluids 20 (8-9), 1081–1106.

Manzari, M. T., Regueiro, R. A., 2005. Gradient plasticity modeling of geomaterials in a meshfree environment. part i: Theory and variational formulation. Mechanics Research Communications 32 (5), 536–546.

Moës, N., Belytschko, T., 2002. Extended finite element method for cohesive crack growth. Engineering fracture mechanics 69 (7), 813–833.

Mohammadnejad, T., Khoei, A., 2013. An extended finite element method for hydraulic fracture propagation in deformable porous media with the cohesive crack model. Finite Elements in Analysis and Design 73, 77–95.

Needleman, A., 1988. Material rate dependence and mesh sensitivity in localization problems. Computer methods in applied mechanics and engineering 67 (1), 69–85.

Oliver, J., Huespe, A., 2004. Continuum approach to material failure in strong discontinuity settings. Computer Methods in Applied Mechanics and Engineering 193 (30), 3195–3220.

Oliver, J., Huespe, A., Pulido, M., Chaves, E., 2002. From continuum mechanics to fracture mechanics: the strong discontinuity approach. Engineering Fracture Mechanics 69 (2), 113–136.

Oliver, J., Huespe, A., Samaniego, E., 2003. A study on finite elements for capturing strong discontinuities. International journal for numerical methods in engineering 56 (14), 2135–2161.

Planas, J., Elices, M., Guinea, G., Gómez, F., Cendón, D., Arbilla, I., 2003. Generalizations and specializations of cohesive crack models. Engineering fracture mechanics 70 (14), 1759–1776.

Regueiro, R., Fossum, A., Jensen, R., Foster, C. D., Manzari, M., Borja, R., 2005. Computational modeling of fracture and fragmentation in geomaterials. SAND2005-5940, Sandia National Laboratories.

Regueiro, R., Foster, C. D., 2011. Bifurcation analysis for a rate-sensitive, non-associative, three-invariant, isotropic/kinematic hardening cap plasticity model for geomaterials: Part i. small strain. International Journal for Numerical and Analytical Methods in Geomechanics 35 (2), 201–225.

Sancho, J. M., Planas, J., Cendón, D. A., Reyes, E., Gálvez, J., 2007. An embedded crack model for finite element analysis of concrete fracture. Engineering Fracture Mechanics 74 (1), 75–86.

Shi, C., van Dam, A. G., van Mier, J. G., Sluys, B., 2005. Crack interaction in concrete. Materials for Buildings and Structures, Volume 6, 125–131.

Simo, J. C., Oliver, J., Armero, F., 1993. An analysis of strong discontinuities induced by strain-softening in rate-independent inelastic solids. Computational mechanics 12 (5), 277–296.

Strouboulis, T., Babuška, I., Copps, K., 2000. The design and analysis of the generalized finite element method. Computer methods in applied mechanics and engineering 181 (1), 43–69.

Weed, D. A., Foster, C. D., Motamedi, M. H., 2015. A combined opening-sliding formulation for use in modeling geomaterial deformation and fracture. Computational Mechanics, in review.

Zi, G., Belytschko, T., 2003. New crack-tip elements for xfem and applications to cohesive cracks. International Journal for Numerical Methods in Engineering 57 (15), 2221–2240.